

THESIS

EFFECTS OF INLET/OUTLET LOCATIONS AND INFLUENT TEMPERATURE ON
HYDRAULIC DISINFECTION EFFICIENCY IN CONTACT TANKS

Submitted by

Yishu Zhang

Department of Civil and Environmental Engineering

In partial fulfillment of the requirements

For the Degree of Master of Science

Colorado State University

Fort Collins, Colorado

Fall 2017

Master's Committee:

Advisor: S. Karan Venayagamoorthy

Jorge A. Ramirez
Ashok Prasad

Copyright by Yishu Zhang 2017

All Rights Reserved

ABSTRACT

EFFECTS OF INLET/OUTLET LOCATIONS AND INFLUENT TEMPERATURE ON HYDRAULIC DISINFECTION EFFICIENCY IN CONTACT TANKS

This study focuses on understanding the effect of inlet/outlet locations and influent temperature on hydraulic disinfection efficiency of drinking water contact tanks for small systems. Computational fluid dynamics (CFD) simulations of flow and scalar transport in a concrete rectangular tank with three inlet/outlet location configurations were performed. The temperature of the influent into the system was varied in the second part of this study in order to explore the effects of temperature gradients on the flow and scalar transport. Hydraulic disinfection efficiencies were computed through the use of residence time distribution (RTD) curves obtained from the CFD simulations and the baffling factor (BF). The physical tank that was used for all tracer tests is located at the Hydraulics Lab at Colorado State University's Engineering Research Center (ERC) in Fort Collins. The rectangular concrete tank was initially constructed with a bottom inlet and top outlet configuration and has a total volume of 1500 gallons. After the CFD simulation results were validated using tracer tests, two principle objectives were investigated using CFD simulations.

First, the effect of inlet/outlet locations and their respective sizes were investigated. For a given constant temperature for both the inflow and ambient water in the tank, three inlet/outlet location combinations (i.e. bottom inlet-bottom outlet, bottom inlet-top outlet, and top inlet-bottom outlet) with two different outlet sizes (i.e. 2-in.-diameter and 4-in.-diameter) were modeled using 15 CFD simulations. Both baffled and un-baffled tanks were modeled. The results

show that a small modification of the outlet pipe diameter results in minor changes in the baffling factor and hydraulic disinfection efficiency. All adjusted un-baffled tanks (i.e. with the three different inlet/outlet configurations) did not yield any satisfactory disinfection performance due to the severe short circuiting that occurs in the tank. The main finding is that for baffled tanks, the top inlet-bottom outlet configuration performed the best and increased baffling factor by over 30% relative to the bottom inlet-bottom outlet configuration for the baffled tank which is commonly found in praxis.

Second, the effect of buoyancy that can occur in disinfection tanks due to drastic temperature differences between the inflow and the ambient water in the contact tank was investigated. Only negatively buoyant conditions were studied in this research. Temperature differences of 0°C, 5°C, 10°C, and 15°C were created by injecting cold inflow to the baffled tanks under two conditions namely: (i) no heat flux condition and (ii) constant wall condition. For the first condition, it was assumed that no heat exchange between tank (and baffle) walls and fluid occurs; while for the second condition, the wall temperature was held constant at 20°C. Both conditions were simulated at different flow rates to capture flow regimes ranging from laminar to turbulent. It was found that the baffling factor varied significantly between laminar, transitional, and turbulent flows. The best hydraulic disinfection efficiency was achieved when the flow was laminar. For no heat flux condition, the effects of the buoyancy increased baffling factor by 57% compared to the base case with no temperature difference. On the other hand, for turbulent flow conditions with a strong temperature difference, the baffling factor reduced by 49% compared to the base case. The constant wall temperature condition produced similar results, but with a smaller change in baffling factor. From a hydrodynamic analysis of the flow fields obtained from CFD simulations, it was concluded that buoyancy could either increase

hydraulic disinfection efficiency or decrease it, depending on the flow regime. Hence, care should be exercised to avoid flows in transitional to turbulent regimes because the negative buoyancy could decrease the baffling factor and lead to inadequate microbial deactivation.

ACKNOWLEDGEMENTS

First, I would like to thank my advisor, Dr. Subhas Karan Venayagamoorthy for his help during both my undergraduate and graduate studies. Being a dedicated and effective educator, he continuously encourages and motivates me to achieve my goal of graduating with my master's degree. Without his guidance and expertise, I would not be able to complete this thesis and other related papers. Aside from his academic assistance to me, I am also influenced by his life philosophy. He knows how to challenge his students and always exhibits an enthusiasm for those challenges. I would also like to thank my committee members, Dr. Jorge Ramirez and Dr. Ashok Prasad, for their support and for providing valuable insight, advices, and comments.

Next, I would like to thank my parents, Yongqiang Zhang and Lixia Sun, for their support. Their constant love and care have encouraged me to overcome the difficulties in my life. They have sacrificed many things in helping me pursue my education. Their support has given me the motivation to perform better.

Additionally, I would like to thank Jeremy Carlston who has given me a lot of guidance when I started my research. He showed me the concrete tank at ERC and taught me how to work with the equipment. He also tutored me on getting started with the CFD simulations when I was struggling.

Finally, I would like to thank the members in the Environmental Fluid Mechanics Research Lab at CSU – Jian Zhou, Amrapalli Garanaik, Oladapo Aseperi, and Jessica Baker – who were all willing to give a hand whenever I needed help.

TABLE OF CONTENT

ABSTRACT.....	ii
ACKNOWLEDGEMENTS.....	v
CHAPTER 1: INTRODUCTION.....	1
1.1 Background.....	1
1.2 Objectives.....	4
1.3 Organization of Thesis.....	4
1.4 New Contribution.....	5
1.5 Research Publication.....	5
CHAPTER 2: LITERATURE REVIEW.....	7
2.1 Small Drinking Water Systems.....	7
2.2 Water disinfection.....	8
2.3 Parameters of System Performance.....	9
2.3.1 Residence Time Distribution.....	10
2.3.2 Theoretical Detention Time.....	10
2.3.3 Baffling Factor.....	11
2.4 Computational Fluid Dynamics.....	12
2.4.1 Numerical Methods.....	12
2.4.2 Governing equations.....	13
2.4.3 Limitations.....	15
2.5 Turbulence Modeling.....	15
2.5.1 DNS.....	17
2.5.2 LES.....	17
2.5.3 RANS.....	18
2.6 Scalar Transport Modelling.....	20
2.7 Buoyancy.....	21
2.7.1 Stratification.....	21
2.7.2 Boussinesq approximation.....	22
2.8 Commercial CFD Software.....	23

2.8.1 ANSYS Workbench	24
2.8.2 FLUENT	24
CHAPTER 3 INLET/OUTLET LOCATION.....	28
3.1 Introduction	28
3.2 Tank Geometry and CFD Validation	29
3.3 Numerical Framework.....	34
3.3.1 Flow dynamics and scalar transport	34
3.3.2 Computational methodology	35
3.4 Results	37
3.4.1 Baffled tanks.....	37
3.4.2 Un-baffled tanks	42
3.5 Discussion	42
3.5.1 Velocity magnitude analysis.....	42
3.5.2 Velocity contour analysis	44
3.6 Conclusion.....	47
CHAPTER 4 BUOYANCY EFFECT	48
4.1 Introduction	48
4.2 Description and Motivation behind Buoyancy Effect.....	49
4.3 Methodology	50
4.3.1 Geometry description	50
4.3.2 Scenario description	52
4.3.3 Numerical model	53
4.4 Results and Discussion.....	57
4.4.1. RTD curves for 5°C influent temperature	57
4.4.2 Flow pattern	69
4.5 Conclusion.....	79
CHAPTER 5 SUMMARY AND CONCLUSIONS	81
5.1 Summary of Research	81
5.2 Major Conclusions	82
5.3 Recommendation for Further Work	83
REFERENCE.....	84

APPENDIX A..... 88

CHAPTER 1: INTRODUCTION

1.1 Background

Water is a precious and ubiquitous resource on the Earth and wherever water flows on this planet, there is a high probability that life can be found. All lifeforms that have been discovered have water as a basic building block with some organisms composed of up to 95% water. Since ancient times, civilizations have always established themselves near water sources because of its necessity for the sustenance of life. However, waterborne illnesses are known to make people sick and have been responsible for high mortality rates in humans. Dating as far back as 4000 B.C., people in ancient Greece and Sanskrit were educated in sand and gravel filtration, boiling, and straining of water. Without knowing about microorganisms, or chemical contaminants, they treated the water mainly due to the resulting enhanced taste. In 1500 B.C. the Egyptians first discovered the principle of coagulation (EPA 2000). Of course, the water treatment technology has evolved considerably over the centuries. In 1804 the first actual municipal water treatment plant designed by Robert Thom, was built in Scotland, ushering in the era of slow sand filtration in Europe. British scientist John Snow was the first to use chlorine to purify water in 1854. In the 1890s, waterborne illnesses became less and less common as chlorination of water gained acceptance throughout the world. But the victory obtained by the invention of chlorination did not last long. With time, the negative effects associated with chlorination (i.e. disinfection by products - DBPs) were discovered when the water is over-disinfected, and hence some alternative water disinfectants were considered. In the United States, beginning in 1914, drinking water standards were implemented for water supplies in public traffic, based on coliform growth. However, it would take until the 1940s before drinking

water standards applied to municipal drinking water. In 1972, the Clean Water Act was passed in the United States. In 1974 the Safe Drinking Water Act (SDWA) was formulated (Lenntech 2005).

Nowadays, in the United States, water quality regulations are developed and administered by the United States Environmental Protection Agency (USEPA). The USEPA was established late in 1970 to ensure human health and environmental protection by a variety of federal research, monitoring, standard-setting and enforcement activities. In the drinking water disinfection aspect, the *Disinfection Profiling and Benchmarking Technical Guidance Manual* provides public water systems and States with USEPA's current technical and policy recommendations for complying with the disinfection profiling and benchmarking requirements of the *Long Term 1 Enhanced Surface Water Treatment Rule (LT1ESWTR)*. This document demonstrates that if a system is required to complete a disinfection profile, it must calculate the CT value for each disinfection segment. CT value is the product of the disinfectant concentration and contact time. A CT value must be met or exceeded based on a desired level of microbial inactivation. Mathematically, given a CT value, a longer contact time allows for the use of lower disinfectant dosage at the inlet to the contact tank. However, if one simply increases the dosage of the disinfectant, undesirable disinfection byproducts could reach unacceptable levels. On the other hand, the water could also become microbial inactive if the contact time is inadequate. In order to estimate the hydraulic disinfection efficiency for a drinking water disinfection system, USEPA (2003) developed a well-known parameter known as the *baffling factor (BF)*. The BF is quantified as t_{10}/TDT , where t_{10} is the time taken to observe ten percent of the inlet concentration at the outlet and TDT is called theoretical detention time which is calculated by dividing the volume of a system by the system flow rate (V/Q). USEPA (2003) also documented a general

baffling factor description chart (see Table 1.1). However, this table is highly inaccurate and difficult to use without proper physical tracer testing. It also failed to consider critical components of design (i.e. inlet configurations and locations, packing material installations) and environmental conditions (e.g. temperature differences between inflow and ambient water). Besides baffling factor, the residence time distribution (RTD) curve is used to estimate the hydraulic disinfection efficiency of a drinking water disinfection system. It shows the outlet concentration of a continuously injected disinfectant as a function of time. Baffling factor can be obtained from RTD curve as highlighted in Figure 1.1.

Table 1.1 Baffling Classification Table (USEPA, 2003)

Baffling Condition	Baffling Factor	Baffling Description
Un-baffled (mixed flow)	0.1	None, agitated basin, very low length to width ratio, high inlet and outlet flow velocities.
Poor	0.3	Single or multiple un-baffled inlets and outlets, no intra-basin baffles.
Average	0.5	Baffled inlet or outlet with some intra-basin baffles.
Superior	0.7	Perforated inlet baffle, serpentine or perforated intra-basin baffles, outlet weir or perforated launders.
Perfect (plug flow)	1.0	Very high length to width ratio (pipeline flow), perforated inlet, outlet, and intra-basin baffles.

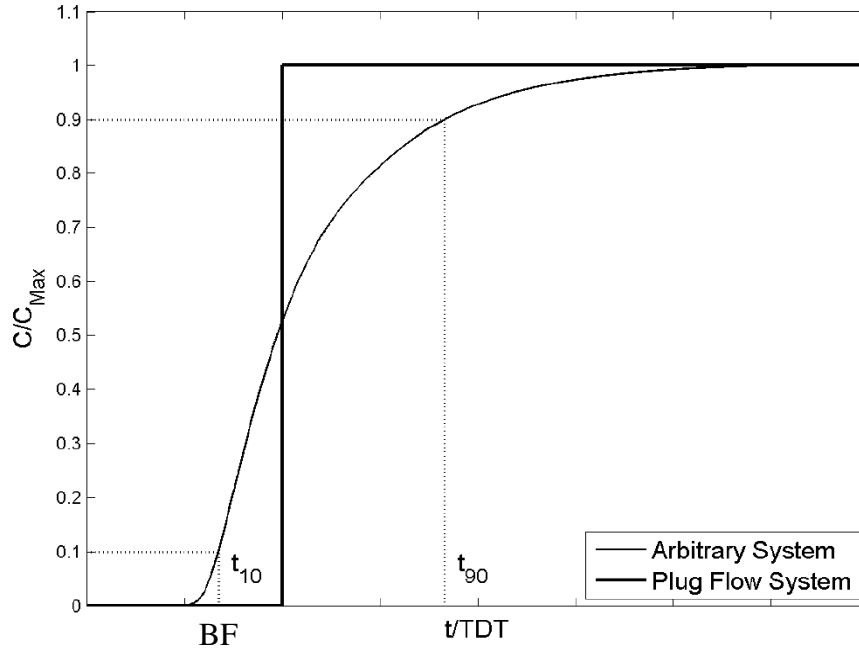


Figure 1.1 RTD Curves for an Arbitrary versus an Idealized System

1.2 Objectives

The main objective of this thesis is to investigate approaches that can optimize the hydraulic disinfection efficiency of contact tanks, especially for small drinking water systems. In contrast to related studies done on this topic, this thesis focuses on the understanding effects of varying the location of inlet and outlets of the tank as well as due to buoyancy that results from temperature differences between influent and ambient water in the tank.

1.3 Organization of Thesis

The technical content of this thesis has been arranged into four further chapters. Chapter 2 is intended to provide a summary of relevant literature review, more detailed definitions of the basic parameters, motivations, and other related knowledge concerning the research. The majority of the results from this research study are presented in Chapter 3 and Chapter 4. Hydrodynamic analysis of CFD simulations are also discussed to provide insights on flow patterns in the modeled systems. In particular, Chapter 3 presents the CFD study to explore the effect of inlet/outlet location and size on hydraulic disinfection efficiency of contact tank.

Results from 15 simulations of flow and scalar transport in a concrete rectangular tank with various inlet/outlet location configurations and two different outlet sizes (i.e. 2-in.-diameter and 4-in.-diameter) are presented. Chapter 4 presents the impact of temperature differences between influent and storage water on baffling factor in the contact tank. The buoyancy effect due to temperature differences, flow rate, and tank configuration, are investigated. Chapter 5 concludes this thesis by summarizing the study in Chapter 3 and Chapter 4. Key findings are highlighted and directions on future work are also indicated.

1.4 New Contribution

The work presented in this thesis makes the following meaningful and original contributions to research on disinfection contact tanks:

- The results clearly highlight the impact of inlet/outlet location of disinfection contact tank. The inlet/outlet location configuration can significantly affect the hydraulic disinfection efficiency, especially when buoyancy effects are important.

To the knowledge of the author, this is probably the first study that investigates the effect of buoyancy on hydraulic disinfection efficiency. The results show that the baffling factor can be considerably lower compared (especially under turbulent flow conditions) compared to flow conditions with constant water temperature. It is important to account for such effects in order to avoid inadequate disinfection of the source water.

1.5 Research Publication

Chapter 3 of this thesis contains substantial portions of a paper by *Zhang and Venayagamoorthy* titled *Effects of Inlet/Outlet Location and Size Influence on baffling factors in Contact Tanks* that will be submitted shortly to the Journal: *American Water Work Association (AWWA)*. The contents of this chapter have also been accepted for presentation at the

Environmental Water Resources Institute (EWRI) World Environmental and Water Resources Congress, May 22-27, 2017 and the Hydrology Day at Colorado State University, March 20-22, 2017. The work presented in Chapter 4 will be submitted to Environmental Science & Technology (ES&T).

CHAPTER 2: LITERATURE REVIEW

2.1 Small Drinking Water Systems

Under the Safe Drinking Water Act (SDWA) in 1974, small public water systems are characterized as systems serving less than 10000 people, but this category represents more than 92% of the nation's public water systems. Thus, small public water systems were further classified into three subcategories i.e. 3,301 – 10,000 persons, 501 – 3,300 persons, and those serving 500 persons or fewer (USEPA, 2006). Broadly speaking, USEPA simply considers any public water system as small if it serves fewer than 3,300 people (USEPA, 2012). Due to the size of the population served, such small systems face unique financial and operational challenges in providing drinking water that meets USEPA standards. Hence, in 1996, small system variances (SSV) were introduced to allow a small system to use a variance technology that is affordable and protective of public health. The technology should also meet the requirement suggested by the regulation. However, the SDWA specifically does not allow small system variances for the microbial contaminants (USEPA 2006). In May, 2003, The Long Term 1 Enhanced Surface Water Treatment Rule (LT1ESWTR) was built to specify treatment requirements to address microbial contaminants in small water systems, but some methods documented in this rule are ambiguous and idealized. Practical cases will generally tend to be under conservative. Therefore, the study in this thesis highlights the scenarios that are often ignored in traditional design methodologies and intends to provide more practical conditions that should be considered in design and operation of small drinking water systems. Oftentimes, innovative treatment technologies are reluctantly accepted by small communities and their state primacy agencies due to potential hidden cost and (perceived) unforeseen health consequences for the community

(USEPA 2016). Therefore, the cost-effective technologies tested by reliable methods are necessary to be suggested and promoted for use in small drinking water systems.

2.2 Water disinfection

One of the concerning issues of drinking water systems is waterborne illness which results from contaminants in source water or treated water. Current treatment includes the use of disinfectant (i.e. chlorine) which can lead to disinfection by-products (DBPs). Although UV treatment, monochloramine, and other disinfectants have been suggested by USEPA as effective agents in disinfection systems, chlorine is the most common disinfectant currently used in the United States and worldwide, especially in small water systems (World Chlorine Council, 2008). Because chlorine is cost-effective, widely accepted and well-established in multiple guidelines by USEPA, this study considered chlorine as a conservative tracer in disinfection systems. In order to qualify the disinfection effectiveness, USEPA (2003) demonstrates that the treated water from an operational drinking water disinfection system must meet or exceed a given CT value based on a desired level of microbial inactivation. CT value simply stands for the product of concentration (C) and contact time (T). CT values are found to be sensitive to pH levels and temperature as they affect the disassociation of chlorine in water (Letterman, 1999). Under a specific condition (i.e. pH and temperature T_o), Davis and Cornwell (2008) provide an empirical approximation to the CT as follows

$$CT = 0.9847C^{0.1758}pH^{2.7519}T_o^{-0.1467}, \quad (2.1)$$

where C is the chlorine's concentration in mg/L, T_o is temperature of water in degrees Celsius. As for the left hand side in equation (2.1), in practice, C is the disinfectant residual concentration measured in mg/L at peak hourly flow and T is the contact (residence) time. However, the objective measurement of contact time T can be ambiguous. USEPA (2003) thus proposed that

t_{10} which is the time it takes to observe 10% of the inlet concentration at the outlet as the relevant contact time. Desired levels of microbial inactivation are also proposed by USEPA (2003), such that the log inactivation (LI) of viruses must be calculated if the system uses ozone, chloramines, or chlorine dioxide for primary disinfection. The LI is defined as follows:

$$\text{Log inactivation} = \log\left(\frac{\text{Influent Contaminant Concentration}}{\text{effluent Contaminant Concentration}}\right) \quad (2.2)$$

Equation (2.2) implies that one log reduction means that 90% of the microorganisms are removed or inactivated, two log corresponds to 99%, three log corresponds to 99.9%, and so on. CT tables that are established by EPA are used to determine the required CT value for a certain level of inactivation. This required CT value also depends on the type of disinfectant.

2.3 Parameters of System Performance

Hydraulic disinfection efficiency is a terminology that is often used to assess the disinfection capability of a water treatment system. Due to the relatively short residence times that the water spends in a contact tank, chemical and biological reaction processes are typically not considered to influence the hydrodynamics as well as the decay of the scalar (tracer) injected into the tank. Therefore, biochemistry reactions are not further discussed in this thesis. Plug flow was defined by USEPA (2003) as water flow that travels through a basin, pipe, or unit process in such a fashion that the entire mass or volume is discharged at exactly the theoretical detention time (TDT) of the unit. Such a condition is ideal for disinfection process because it leads to advection-dominated transport. However, few systems in practice are able to achieve plug flow. The uneven flow path in the systems could result in short-circuiting and dead zones (Wilson & Venayagamoorthy, 2010; Wilson, 2011), which would reduce the hydraulic disinfection efficiency of a system.

2.3.1 Residence Time Distribution

Residence time distribution (RTD) curves provide key information on the distribution of a scalar and hence are used to assess the hydraulic disinfection efficiency of a contact tank. The shape of the curve provides insight to the nature of the flow in the system. For example, a steeper gradient in a RDT curve represents a flow condition closer to plug flow that is dominated by advection and a flatter gradient represents a flow condition further from plug flow that is dominated by turbulent diffusion. Thus, in disinfection systems, the RTD curve can be used to predict the overall microbial inactivation levels and the formation of disinfection by-products (DBPs). A perfect plug flow produces a square-like RTD curve where the normalized concentration at the outlet jumps instantaneously from 0% to 100% at the system's TDT (as shown in Figure 1.1). In practical systems, the earlier rising limb of the RTD curve implies the possibility of inadequate microbial inactivation, while later parts of the curve can potentially lead to recirculation of flow. For a typical RTD curve for a real system, a flat curve normally appears in the early and later parts of the RTD curve, and a much steeper curve is observed in the middle section (see Figure 1.1).

2.3.2 Theoretical Detention Time

The well-known theoretical detention time (TDT) is defined as the ratio of the volume of the fluid in the tank V to the steady volumetric flow rate Q (equation 2.3). In an ideal case (i.e. perfect plug flow), all fluid parcels entering the tank would have identical residence times since they pass through the entire volume of the system as plug. However, in a real system, given a steady volumetric flow rate Q at the inlet, some of the fluid parcels would find a shorter way to flow through the reactor (i.e. short-circuiting), while others may stay longer in the tank due to

recirculation caused by flow separation in some sections of the reactor (i.e. dead zones). Hence, their residence times would be quite varied from the theoretical detention time (TDT).

$$TDT = \frac{V}{Q} \quad (2.3)$$

2.3.3 Baffling Factor

In the United States, the most common parameter that quantifies the hydraulic disinfection efficiency is the baffling factor (BF). It is the ratio of an approximated contact time to the theoretical detention time (TDT) of a given system given by

$$BF = \frac{t_{10}}{TDT} \quad (2.4)$$

The approximated contact time is usually taken as t_{10} which is the time required for 10% of the inlet tracer concentration to reach the outlet. Therefore by definition, the range of baffling factor is between 0 to 1. A disinfection tank which functions in a strictly plug flow manner has the highest hydraulic disinfection efficiency (i.e. BF=1). In a disinfection system, a baffling factor that is closer to 1 indicates higher hydraulic disinfection efficiency.

2.3.4 Morrill Index

Even though the baffling factor is prevalent in the nation and most documents from USEPA have utilized this number to evaluate the hydraulic disinfection efficiency, the shortcomings of the BF should not be ignored. Wilson and Venayagamoorthy (2010) claimed the use of BF inherently assumes that plug flow could be achieved due to the use of TDT. Since it only includes t_{10} in the formula, BF is a short-circuiting indicator. The Morrill Index (MI), on the other hand, used as a measure of hydraulic efficiency in Europe, evaluates the amount of dispersion in a system based on the ratio $\frac{t_{90}}{t_{10}}$. It can be thought of as a measure of dispersion occurring in the contact tank (Teixeira & Siqueira, 2008). As with the baffling factor the best

case is $MI = 1$ corresponding to plug flow but can reach much larger values depending on the amount of dispersion that occurs in a given flow system.

2.4 Computational Fluid Dynamics

Computational fluid dynamics (CFD) is a branch of fluid mechanics that has gained momentum over the last few decades (Moin, 2010). It uses numerical methods and algorithms to solve and analyze problems that involve fluid flows. Knowledge of mathematics and computer science is required to apply CFD. This method combines pure experiment and pure theory together. Experiments can provide useful and reliable results of a given physical phenomenon at work but are often considered to be expensive and labor-intensive. On the other hand, theoretical methods can provide a basic overview of complex fluid dynamics problems but due to simplifying assumptions usually fail to provide a complete understanding of the problem. CFD has the advantages from both methods as it solves the physical problem numerically. Besides, CFD can also model physically impossible conditions, such as inviscid flows. However, one should always be cognizant of the fact that when assessing a numerical method, uncertainties and errors are inevitable from issues such as improper numerical discretization of equations, using inappropriate averaged parameters, and simplifying assumptions, etc. (See 2.4.3 for a discussion on limitations of CFD). Thus, it is important for the physics behind a problem to be well understood and the results from CFD must be validated before it is applied to new problems.

2.4.1 Numerical Methods

Numerical methods are used to find numerical approximations to the solution of ordinary differential equations (ODEs) or partial differential equations (PDEs). In many cases, the differential equations cannot be solved by analytical methods, thus necessitating the use of numerical methods to obtain sufficiently accurate solutions to such unclosed problems,

especially in engineering. This is achieved through discretization wherein algebraic estimates are substituted for unknown derivatives in a given series of differential equations and the resulting system of algebraic equations are solved computationally (Moin, 2010). Finite element method (FEM), finite difference method (FDM), and finite volume method (FVM) are some of the widely used techniques to perform discretization in numerical methods. As for CFD software, finite volume method (FVM) is widely used because the resulting solution naturally satisfies the conservation of fluid quantities such as mass, momentum and energy. When applying the finite volume method, CFD divides the entire domain into finite smaller volumes cells or meshes. The governing equations of fluid motions are then applied to each volume cell with the overall computational domain constrained by specified boundary and initial conditions.

2.4.2 Governing equations

The fundamental equations for fluid motion are the Navier-Stokes equations which are simply the momentum equations (Eq.2.6). Besides, conservation of mass (Eq.2.5) and energy (Eq.2.7) are also required in order to obtain a complete solution of the flow field. These equations are often simplified using appropriate assumptions. The energy conservation equation is only required when heat transfer is considered (see Chapter 4). Consider a Cartesian coordinate having the z (or x_3) axis orientated vertically upward and the x, y (or x_1, x_2) axes contained in the horizontal plane. The general governing equations are as follows:

$$\frac{\partial p}{\partial t} + \nabla \cdot (\rho \vec{U}) = S_m, \quad (2.5)$$

$$\frac{\partial}{\partial t} (\rho \vec{U}) + \nabla (\rho \vec{U} \cdot \vec{U}) = -\nabla P + \mu \nabla^2 \vec{U} + \rho \vec{g} + \vec{F}, \quad (2.6)$$

$$\frac{\partial}{\partial t} (\rho E) + \nabla \cdot (\vec{U} (\rho E + P)) = \nabla \cdot \left((\Gamma + \Gamma_t) \nabla T - \sum_j h_j \vec{J}_j + \mu \nabla \vec{U} \cdot \vec{U} \right) + S_h, \quad (2.7)$$

where \vec{U} and P are the time and space dependent velocity and pressure. S_m is the mass added to the continuous phase. ρ and μ are the density and dynamic viscosity of the fluid. $\rho\vec{g}$ and \vec{F} are the gravitational body force and external body forces. E is the specific energy of the system. The effective conductivity, $(\Gamma + \Gamma_t)$ is a sum of the molecular conductivity and the turbulent thermal conductivity, and \vec{J}_j is the diffusion flux of species j . The first three terms on the right-hand side of Equation (2.7) represents energy transfer due to conduction, species diffusion, and viscous dissipation, respectively. S_h includes the heat of chemical reaction, and any other volumetric heat sources (ANSYS 2013).

Some terms in the equations can be canceled out due to the following assumptions. In this research study, there are no external force, mass and heat sources, hence \vec{F} , S_m and S_h are set to zero. The fluid is assumed to be incompressible, and hence all density can be factored out of the derivative operator by assuming that water is incompressible and with a constant density of ρ_o for a given temperature. When inlet temperature is different from the temperature of tank storage water, the Boussinesq approximation (See 2.6.2) will be introduced to the flow, and then Navier-Stokes equations will be modified accordingly. In Equation (2.9), the density difference ρ' is defined as $\rho' = \rho_o - \rho$. The simplified governing equations are shown in Equations (2.8) to (2.10). In chapter 3, temperature of the influent and storage fluid is the same, so only modified continuity equation (Eq. 2.8) and Navier-Stokes equation (Eq. 2.9) were applied. In order to account for temperature difference in chapter 4, all three equations (Eq. 2.8, 2.9, 2.10) are solved together.

$$\nabla \cdot \vec{U} = 0 \quad (2.8)$$

$$\frac{\partial}{\partial t}(\vec{U}) + \nabla(\vec{U} \cdot \vec{U}) = -\frac{1}{\rho_o} \nabla P + \nu \nabla^2 \vec{U} + \frac{\rho'}{\rho_o} \vec{g} \delta_{i3} \quad (2.9)$$

$$\rho_o \frac{\partial}{\partial t} (E) + \nabla \cdot (\vec{U}(\rho_o E + P)) = \nabla \cdot \left((\Gamma + \Gamma_t) \nabla T - \sum_j h_j \vec{J}_j + \mu \nabla \vec{U} \cdot \vec{U} \right) \quad (2.10)$$

2.4.3 Limitations

In CFD, numerical analyses including interpolation, numerical differentiation, numerical integration, etc. are used. One should be aware of the errors and uncertainty that are associated with a given numerical method when using a CFD model. The sources of errors could be various. First, the errors could come from truncation error of higher order terms in the Taylor series expansions. Due to the inherently unmanageable nature of an infinite series only the first few terms (i.e. the lower order terms) are used and the rest (i.e. higher order terms or truncation terms) are discarded, resulting in truncation errors (Moin 2010). Second, modeling errors could be another source of error. Consider for example turbulence modeling where a myriad of models have been developed based on their capability of capture pertinent length scales as discussed in section 2.5. Some length scales are necessarily ignored, and thus, errors are therefore inherently introduced. With several assumptions, the exact governing equations are always simplified and computed. Those assumptions and simplifications could also be a source of error. Last but not least, human errors, such as user input mistake, model selection mistake, etc. could also lead to invalid results. Again, due to these errors and uncertainties coming from numerical methods, CFD simulations should be validated before they are used to investigate new problems.

2.5 Turbulence Modeling

Compared to laminar flow which is predictable and orderly, turbulence is characterized as being unsteady, irregular, seemingly random and chaotic (Pope, 2000). The study of turbulent flows is difficult and there are no universal theories of the turbulence phenomenon. Therefore,

the increasing power of digital computers is expected to achieve the objective of modeling the turbulence problem in order to yield meaningful solutions.

In order to understand turbulent flow problems, one needs to distinguish between small-scale turbulence and large-scale motions in such flows. The large-scale motions are influenced by the flow geometry, while the small-scale turbulence maybe considered universal and hence determined by dissipation and viscosity (Pope 2000). In 1941, Kolmogorov originally proposed the now well-known set of hypotheses to categorize the large and small scales and the relationship among length, velocity, and time scales, referred widely to as the Kolmogorov hypotheses.

Length, velocity, and time scales are three essential scales that characterize turbulence. The largest eddies size l_o and its velocity u_o is comparable to the flow length scale L and velocity scale U . The corresponding time scale comes from $\tau_o = \frac{l_o}{u_o}$. It was hypothesized that when those scales are small enough, they are uniquely determined by two parameters: the dissipation rate of turbulent kinetic energy, \mathcal{E} , and viscosity, ν as

$$\eta \equiv \left(\frac{\nu^3}{\mathcal{E}} \right)^{\frac{1}{4}}. \quad (2.11)$$

This length scale is called the Kolmogorov length scale η . The Kolmogorov length scale is characterized as the smallest scale in a turbulent flow. The ratio of the smallest scales to largest scales decreases with increasing Reynolds Number as follows

$$\frac{\eta}{l_o} \sim Re^{-\frac{3}{4}} \quad (2.12)$$

In a fully turbulent flow with a sufficiently high Reynolds number, there is a large range of scales l , that are present in the flow, such that $l_o \gg l \gg \eta$. The difficulty of modeling the turbulence problem lies in capturing all the scales present in the large spectrun. Many turbulence

models are developed based on various capability of capturing different scales. Currently, direct numerical simulation (DNS), large eddy simulation (LES), turbulent-viscosity models, and Reynolds-averaged Navier Stokes Simulations (RANS) are the commonly used approaches to solving turbulent flow problems. The principal criteria to select different models include level of description, completeness, cost and ease of use, range of applicability, and accuracy. The following sections discuss the various numerical simulations techniques used in CFD.

2.5.1 DNS

Direct numerical simulation (DNS) is the most computationally expensive approach that essentially solves the exact (instantaneous) governing equations (i.e. Eq. 2.5, Eq. 2.6, and Eq. 2.7) for all the scales in a turbulent flow. Thus, it is able to provide very detailed insights of the flow. However, DNS yet requires exorbitant computational power. Therefore, it should be appreciated that DNS is limited to flows at low to moderate Reynolds numbers. Hence, DNS is primarily used to attempt and obtain insights on fundamental flow properties.

2.5.2 LES

In large eddy simulation (LES), the small scales are filtered out by decomposing the velocity (or any other flow variable) into a large filtered component and a residual (unresolved) component. Only large-scale turbulent motions, such as large filtered velocity, are solved explicitly and the residual stress tensor is modeled by simple (eddy viscosity type) models (Pope, 2000). Even though LES is considered as another computationally expensive approach, LES does not need nearly as much as computational resources as DNS. High-Reynolds-number flows, thus, could be solved by LES. Due to increasing computing power, LES is more and more popular in many research studies, but it still remain prohibitively expensive for most problems in industry.

2.5.3 RANS

Reynolds averaged Navier-Stokes (RANS) approach uses turbulent-viscosity models and Reynolds stress models to compute the mean flow fields. The corresponding equations solved are known as the Reynolds-averaged Navier-Stokes (RANS) equations. In this framework, the velocity $U(x, t)$ is decomposed into its mean velocity $\bar{U}(x, t)$ and the fluctuation velocity $u(x, t)$ (Eq. 2.13). Similar decomposition is performed on pressure field (Eq. 2.14).

$$U(x, t) = \bar{U}(x, t) + u(x, t) \quad (2.13)$$

$$P(x, t) = \bar{P}(x, t) + p(x, t) \quad (2.14)$$

From continuity equation (Eq. 2.9), the divergence of instantaneous and averaged parameters (i.e. U and P) is zero. Then by subtraction, the divergence of fluctuations is also zero. Substituting the values into Equation 2.9 and Equation 2.10, the Reynolds averaged Navier-Stoke's (RANS) equations are obtained as follows

$$\nabla \cdot \bar{U} = 0. \quad (2.15)$$

$$\frac{\partial}{\partial t}(\bar{U}) + \bar{U}\nabla(\bar{U}) = -\frac{1}{\rho_o}\nabla\bar{P} + \nu\nabla^2\bar{U} - \overline{u_i u_j} + \frac{\rho}{\rho_o}\vec{g}\delta_{i3}. \quad (2.16)$$

Compared to the instantaneous Navier-Stokes equations (equation 2.10), an extra term, $\overline{u_i u_j}$, called the Reynolds stress tensor is on the right hand side of Equation (2.16). This Reynolds stress tensor represents transport of momentum due to turbulent fluctuations. Statistically, it also represents the covariance of the fluctuating velocity field. In a 3D turbulence problem, this Reynolds stress tensor includes six unknown values, and thus, the Reynolds stresses render the turbulence problem unclosed. The modeling of Reynolds stresses are a key problem in RANS based CFD simulations. Many models have been developed parameterize the values of Reynolds stresses.

In turbulent-viscosity models, the Reynolds stresses are usually modeled using the so-called turbulent viscosity hypothesis (TVH) which states that the deviatoric Reynolds stresses are proportional to the mean rate of strain as follows

$$-\rho\overline{u_i u_j} + \frac{2}{3}\rho\kappa\delta_{ij} = \rho\nu_T \left(\frac{\partial\overline{U}_i}{\partial x_j} + \frac{\partial\overline{U}_j}{\partial x_i} \right) = 2\rho\nu_T\overline{S}_{ij}. \quad (2.17)$$

The only unknown value in Equation (2.17), is ν_T , which is the turbulent viscosity. Invoking the TVH reduces the number of unknowns from six to one. The problem then shifts to the prescription of ν_T . For example, the standard k- ϵ model introduces turbulence kinetic energy, k , and its dissipation rate ϵ to obtain turbulent viscosity as

$$\nu_T = \frac{C_\mu k^2}{\epsilon}. \quad (2.18)$$

$$\frac{\partial}{\partial t}(\rho k) + \frac{\partial}{\partial x_i}(\rho k u_i) = \frac{\partial}{\partial x_j} \left[\left(\mu + \frac{\mu_t}{\sigma_k} \right) \frac{\partial k}{\partial x_j} \right] + G_k + G_b - \rho\epsilon. \quad (2.19)$$

$$\frac{\partial}{\partial t}(\rho\epsilon) + \frac{\partial}{\partial x_i}(\rho\epsilon u_i) = \frac{\partial}{\partial x_j} \left[\left(\mu + \frac{\mu_t}{\sigma_\epsilon} \right) \frac{\partial \epsilon}{\partial x_j} \right] + C_{1\epsilon} \frac{\epsilon}{k} (G_k + C_{3\epsilon} G_b) - C_{2\epsilon\rho} \frac{\epsilon^2}{k}. \quad (2.20)$$

C_μ is a constant that has been determined empirically to be close to a value of 0.09 except near the boundaries. In this research study, re-normalization group (RNG) κ - ϵ model was selected where C_μ is derived using RNG theory and a constant value of 0.0845 is obtained. G_k is the generation of turbulence kinetic energy due to the mean velocity gradients. G_b is the generation of turbulence kinetic energy due to buoyancy, σ_k and σ_ϵ are the turbulent Prandtl number for k and ϵ .

Another commonly used RANS model is the Reynolds stress model. This model applies transport equations (equation 2.21) to solve for individual Reynolds stresses. The turbulent viscosity hypothesis thus is not needed.

$$\frac{\partial}{\partial t}(\rho \overline{u_i u_j}) + \frac{\partial}{\partial x_k}(\rho u_k \overline{u_i u_j}) = D_T + D_L + P_{ij} + G_{ij} + \phi_{ij} + \varepsilon_{ij}, \quad (2.21)$$

where D_T , D_L is the turbulent and molecular diffusivity, respectively; P_{ij} is stress production; G_{ij} is buoyancy production, ϕ_{ij} is pressure strain, and ε_{ij} is dissipation. In Equation (2.21), D_L , P_{ij} do not require any modeling, while D_T , G_{ij} , ϕ_{ij} , ε_{ij} need to be modeled to close the problem (ANSYS 2013).

2.6 Scalar Transport Modelling

Gradient-diffusion hypothesis (GDH) and its related ideas are the fundamental concepts governing the scalar transport modeling in this research study. The hypothesis states that the scalar flux vector, $\overline{u\phi}$, is aligned with the mean scalar gradient vector (Pope, 2000), i.e.

$$\overline{u\phi} = -\Gamma_T \nabla \overline{\phi}. \quad (2.22)$$

In equation (2.22), ϕ is a conserved scalar which is neither generated nor destroyed in the process. In this study, the scalar is passive which means that the dynamics of the flow is not affected by the scalar. Here, Γ_T is turbulent diffusivity which is determined as

$$\Gamma_T = \frac{\nu_t}{Sc_t}, \quad (2.23)$$

where Sc_t is called turbulent Schmidt number which generally ranges from 0.18 to 1.34, based on field observations (Flesh 2002). Venayagamoorthy and Stretch (2010) have shown that the turbulent Schmidt number has a value of 0.7 for neutrally stratified flows. Yimer et al. (2002) suggested that for an axisymmetric turbulent free round jet, the optimized Sc_t value is also 0.7. Sc_t values used in several studies are summarized in Table 1 (Yoshihide & Stathopoulos, 2007).

Table 2.1 Sc_t Value Used in Several Studies

Sc_t values	Research Studies
0.63	Lien et al. (2006)
0.7	Li and Stathopoulos (1997), Wang and McNamara (2006)
0.77	Zhang et al. (1996)
0.8	Brzoska et al. (1997)
0.9	Delaunay (1996), Baik et al. (2003), Kim et al. (2003), Santiago et al. (2007)

In Chapter 3, the flow that is investigated is neutrally stratified, hence, Sc_t was set to 0.7. On the other, value of Sc_t is varied to account for buoyancy effects in Chapter 4. For the purpose of this study, residence time distribution (RTD) curves are obtained by monitoring the concentration of a conserved passive scalar at the outlet of the system. The scalar transport of a conservative tracer was modeled using the advection-diffusion equation (Pope 2000) as.

$$\frac{DC}{Dt} = \frac{\partial C}{\partial t} + \bar{U} \cdot \nabla C = \nabla \cdot ((\Gamma + \Gamma_t)\nabla C), \quad (2.24)$$

where C is the average tracer concentration, and Γ is the molecular diffusivity of the passive scalar. Different from turbulent diffusivity (Γ_t) which is a flow dependent quantity, molecular diffusivity (Γ) is a characteristic of the scalar in particular fluid.

2.7 Buoyancy effects

2.7.1 Stratification

A stratified flow may be defined as a flow where the density varies in the vertical direction. Such density variations result in qualitative and quantitative modifications of flow patterns by buoyancy. The density variation could be due to the variation of temperature, salinity, or concentration. Stratification is common in many natural and engineering flow applications, such as turbulence in ocean and lakes, air circulation in atmosphere, and flow in drinking water systems. Three possible stratification regimes can exist namely: stable stratification, unstable stratification, and neutral stratification. Stable stratification forms when

dense fluid is below the light fluid and it will generally suppress vertical mixing of mass and momentum of a system; while unstable stratified flow (i.e. dense fluid above light fluid) increases the mixing by generation of convective vertical motions. The buoyancy effect has not been well studied in many engineering problems, and thus it is usually ignored or overlooked in many engineering applications. However, the buoyancy effect could impact a hydraulic system dramatically in some circumstances and as such should not be neglected. The neutral stratification category is the condition under which the density is constant in the vertical direction. This is the common assumption in many studies, yet is still an ideal condition. In chapter 3 of this thesis, neutral case was assumed and the related results were discussed. In chapter 4, density current was introduced to the system by injecting a cold influent, so the main objective of chapter 4 in this thesis is to provide insight into the fluid mechanics of stratified flows with particular emphasis on turbulence under stratified conditions.

Any current in a fluid that is kept in motion due to differences in horizontal density is called a density current (Cenedese, 2012). Negative buoyancy and positive buoyancy are two primary density currents. If an inflow is less dense than the ambient fluid, it is referred to as positive buoyancy; otherwise, it is called negative buoyancy (Tian & Roberts, 2008). This density difference ($\rho' = \rho_o - \rho$) can be characterized by the modified acceleration due to gravity ($g'_o = g \left| \frac{\rho'}{\rho_o} \right|$, see equation 2.9). Boussinesq approximation will be applied when solving flows with buoyancy problems (See Section 2.7.2 for details).

2.7.2 Boussinesq approximation

As discussed above, water is a very weakly compressible fluid, so it is often defined as incompressible fluid, yet in many engineering applications the water density could vary with temperature and concentration. A very well-known approximation that satisfies the former

requirement and assumes that the fluid is close to incompressibility is the Boussinesq approximation. Although this approximation is widely applied in stratified flows, it is noteworthy that the Boussinesq form of the equations holds under two main assumptions. First, the density difference is small compared to the bulk density of fluid (i.e. $\left| \frac{\rho'}{\rho_o} \right| \ll 1$). Second, the inertial accelerations are small compared to the gravitational acceleration (Armenio & Sarkar, 2005). Equation 2.8 coupled with Equation 2.9 are the equations in Boussinesq form.

The momentum equation (Equation. 2.9) contains a gravitational term $\frac{\rho'}{\rho_o} \vec{g} \delta_{i3}$ that contributes to the enhancement or suppression of momentum depending on whether the flow is stably stratified or unstably stratified. The delta function δ_{i3} is 1 when $i=3$, otherwise it is zero. As already mentioned, ρ' denotes the density fluctuation i.e. $\rho'(x, y, z, t) = \rho_o - \rho(x, y, z, t)$, wherein ρ_o is a constant, bulk density and ρ is the instantaneous density that varies with space and time. When negatively buoyant inflow (i.e. $\rho' < 0$) injects into the system, $\frac{\rho'}{\rho_o} \vec{g}$ is less than 0. Under the assumption of $\left| \frac{\rho'}{\rho_o} \right| \ll 1$ and $\rho \approx \rho_o$, ρ can be replaced by ρ_o in the former two terms of momentum equation, but it certainly cannot be replaced in the modified gravitational acceleration, otherwise the fluid would be homogeneous with a constant density ρ_o (Armenio & Sarkar, 2005).

2.8 Commercial CFD Software

Currently some of the most common CFD codes used in engineering practice include ANSYS, CFD++, CFX, COMSOL Multiphysics, FLOW-3D, PHOENICS, and STAR-CD (CFD Online.com). Considering the purpose of this study, FLUENT by ANSYS was selected for simulations and post processing procedures. Besides, ANSYS Workbench was chosen for geometry and mesh generation in this research study.

2.8.1 ANSYS Workbench

ANSYS Workbench Platform has five common tools and capabilities, such as ANSYS CAD connections, ANSYS Meshing, ANSYS DesignModeler, ANSYS DesignXplorer, and FE Modeler (ANSYS, 2009). ANSYS CAD connections and ANSYS Meshing are used as preprocessing procedures. ANSYS CAD connection was used to create the system geometry. It has the ability to handle all major computer-aided-design (CAD) systems. The Named Selection Manager can be used to create custom attributes within the CAD system and use them directly in ANSYS application for meshing, modeling, and analysis. After creating the geometry, the computational mesh can be generated by ANSYS Meshing, including global and local mesh controls. Global mesh controls are used to create the general meshing strategy. Global settings are categorized into defaults groups (i.e. physics and solver preference), sizing group, inflation group, other assembly meshing group of controls (i.e. None, Cutcell, and Tetrahedrons), statistics analysis, etc. Instead of applying to entire geometry, local mesh controls are able to apply on a highlighted portion. The following local mesh controls are available: sizing control, refinement control, method control, inflation control, mapped face control, etc. These tools make it more automated to balance the requirements and obtain the right mesh. Many mesh types (i.e. tetrahedral, hexahedral, polyhedral, pyramid, wedge, and cut cells) make them fit in various unstructured geometry easily, and these geometry input data is preserved in FLUENT. Due to the specific geometry of the modeled rectangular tank, Cutcell meshes were applied in this study.

2.8.2 FLUENT

ANSYS FLUENT has the ability to solve a wide range of incompressible and compressible, laminar and turbulent fluid flow problems. Both steady and transient state simulations can be performed for complex geometries using broad range of mathematical models

for transport phenomena, such as scalar and heat transfer. For all flows, ANSYS FLUENT solves conservation equations for mass (i.e. continuity equation) and momentum (Navier-Stokes equation). For flow involving heat transfer, an additional equation for energy is solved. Extra equations are also solved when the flow is turbulent. The equations that are expected to be solved in the simulations are controlled by various solvers and models built in FLUENT (See 2.8.2.1 and 2.8.2.2).

2.8.2.1 Selection of Numerical Methods

ANSYS FLUENT has two numerical methods (solvers) which are pressure-based solver and density-based solver. Generally speaking, pressure-based solver is favorable for low-speed incompressible flows, while density-based solver is developed for high-speed compressible flow. Both solvers apply Navier-Stokes equations to obtain the velocity field, using different approaches. For this study, the fluid (water) is assumed to be incompressible and the flow is slow, hence the pressure-based solver was selected. Pressure-based techniques solve the equations sequentially. Several pressure-velocity coupling algorithms are included in FLUENT, including SIMPLE, SIMPLEC, PISO, and fractional step methods. The SIMPLE (Semi-Implicit Method for Pressure-Linked Equations) algorithm was used for pressure-velocity coupling for all simulations performed in this thesis. With this algorithm, the governing equations are first discretized. Pressure values are then interpolated by standard scheme. Other variables such as momentum, energy and scalar, etc. are interpolated by first order upwind scheme. Additionally, the discretized equations are coupled with velocity. A specific relationship between velocity and pressure is corrected by SIMPLE algorithm to satisfy mass conservation and to obtain the pressure field.

2.8.2.2 Selection of models

Varieties of turbulent models are built in FLUENT, such as Spalart-Allmaras model, standard, RNG, Realizable κ - ε model, standard and SST κ - ω model, Reynolds stress model, LES model, etc. This study used the RNG κ - ε model for all the simulations. RNG κ - ε model is a variant of the standard κ - ε models in which the TVH is used to determine turbulent viscosity and hence the Reynolds stresses. In addition to invoking the TVH, the κ - ε models consist of two model transport equations for κ and ε , and the specification of the turbulent viscosity (Eq. 2.17) (Pope, 2000). Compared to the standard κ - ε model, the re-normalization group (RNG) κ - ε model has an additional term, R_ε in its ε equation which improves the accuracy for rapidly strained flow (See Eq. 2.25). It also includes the swirl effect in turbulence (See Eq. 2.26).

$$\frac{\partial}{\partial t}(\rho\varepsilon) + \frac{\partial}{\partial x_i}(\rho\varepsilon u_i) = \frac{\partial}{\partial x_j} \left[\left(\mu + \frac{\mu_t}{\sigma_\varepsilon} \right) \frac{\partial \varepsilon}{\partial x_j} \right] + C_{1\varepsilon} \frac{\varepsilon}{k} (G_k + C_{3\varepsilon} G_b) - C_{2\varepsilon} \rho \frac{\varepsilon^2}{k} - R_\varepsilon \quad (2.25)$$

Compared to the standard ε equation, the additional term in RNG ε equation is given in equation (2.26).

$$R_\varepsilon = \frac{C_\mu \rho \xi^3 \left(1 - \frac{\xi}{\xi_0} \right) \varepsilon^2}{1 + \beta \xi^3} \frac{\varepsilon^2}{k}, \quad (2.26)$$

wherein $\xi \equiv \frac{Sk}{\varepsilon}$, $\xi_0 = 4.38$, $\beta = 0.012$. ξ represents the strain of a flow. RNG κ - ε model also modifies turbulent viscosity by accounting for the effects of swirl or rotation (See Eq. 27).

$$\mu_t = \mu_{t0} f \left(\alpha_s, \Omega, \frac{k}{\varepsilon} \right), \quad (2.27)$$

where μ_{t0} is the value of turbulent viscosity calculated without the swirl modification (See Eq. 2.17), α_s is a constant determined by the swirl condition. Thus, the RNG κ - ε model works better for rapidly strained and swirl flow. Besides, the RNG κ - ε model is also better for low-Reynolds number flows (ANSYS, 2013).

To the specific problem of disinfection tank in small drinking water systems, swirling and rapidly strained flows are very likely to occur near the inlet jet and the Reynolds number is expected to be relatively small due to low flow rate. Taking into consideration the specified conditions, computational cost, and accuracy, re-normalization group (RNG) κ - ϵ model was selected to solve the problems described in chapter 3 and chapter 4.

CHAPTER 3 INLET/OUTLET LOCATION¹

3.1 Introduction

As alluded to in the discussion in chapter 2, Chlorine is one of the most common methods employed for drinking water treatment in the United States (World Chlorine Council, 2008). However, it might not be effective in disinfection due to either inadequate microbial inactivation or carcinogenic disinfection by-products (DBPs) (Xu 2010 & Wang et al. 2003). Small drinking water systems, which are defined as serving fewer than 3300 people (USEPA 2014), often do not meet the minimum water quality standards set by USEPA due to lack of financial and human resources. Often, small drinking water disinfection systems are poorly designed (e.g. poor inlet conditions, short-circuiting, and dead zones), and hence are vulnerable to health risks associated with poor drinking water disinfection. According to the USEPA, even though small drinking water systems serve only 18% of the population in the United States, they are responsible for 94% of all violations for exceeding allowable maximum contaminant levels (USEPA 2011). Therefore, it is important to draw public attention to drinking water safety in small and urban areas and to investigate cost-effective and efficient design of small disinfection systems.

A contact tank with high hydraulic disinfection efficiency implies that the flow is dominated by advection with negligible diffusion, fewer dead zones, and less short-circuiting. Previous studies have shown a number of approaches to improve hydraulic disinfection efficiency. For example, the placement of baffles inside a contact tank is known to significantly reduce the amount of short-circuiting leading to high hydraulic disinfection efficiency (Xu 2010). Another approach is the use of packing material to promote uniform flow conditions and hence increase the contact time (Barnett et al. 2014). Yet another approach involves some simple

¹ The content of this chapter has submitted to AWWA.

modifications to inlet orientation (e.g. the use of a Tee attachment to a sharp inlet) which can lead to quicker homogenization of longitudinal velocities to positively impact the hydraulic disinfection efficiency (Carlston & Venayagamoorthy 2015). High hydraulic disinfection efficiency could be also achieved by adjusting the length of baffle turn opening to the width of baffle channels to be close to one in order to encourage the flow transport through advection (Taylor et al. 2015). Although Wright & Hargeeaves (2001) and Rodrigo et al. (2007) have mentioned the sensitivity of flow dynamics to inlet configuration and location on un-baffled tanks, a more comprehensive study that focuses on the size and location of the inlet and outlet of contact tanks using CFD simulation is still necessary. Therefore, the main objective of this chapter is to study how to explore ways to increase hydraulic disinfection efficiency of contact tanks by analyzing the effects of inlet/outlet location and size.

3.2 Tank Geometry and CFD Validation

In order to understand the effect of inlet/outlet size and location on hydraulic disinfection efficiency of contact tanks, computational fluid dynamics (CFD) model as well as a series of results from physical experiments were utilized. A concrete rectangular disinfection tank which is located at the Hydraulics Laboratory in the Engineering Research Center at Colorado State University in Fort Collins was used for physical tracer studies. This tank was constructed with a 2-in.-diameter bottom inlet and a 4-in.-diameter top outlet. Figure 3.1 shows a schematic of the rectangular tank. All dimensions are shown in inches. This tank has a volume of approximately 1500 gallons. Two baffle walls divide the tank into three channels. The inlet is located in the lower left corner at the bottom of the first channel, while the outlet is located in the upper right corner at the top of the third channel (see Figure 3.1). In order to be cost-effective and to avoid additional physical tracer tests, CFD simulations were utilized to explore the flow dynamics and

hydraulic disinfection efficiency for different inlet/outlet configurations to that shown in Figure 3.1. For example, By the inlet to the tank can be easily moved to the top and outlet can be relocated to the bottom in the CFD model in order to investigate the influence of the location on the hydraulic disinfection efficiency. Similarly, the outlet size can also be easily modified in the simulations. To constrain the study, all inlets and outlets were modeled as 2” diameter sharp entry and exit pipes and tested at flow rates of 10 gpm, 20 gpm, and 40gpm, respectively. Further, tank with an enlarged 4” diameter outlet (not shown in figures) was also tested but only at a flow rate of 20 gpm. Figure 3.2(A) shows a contact tank with both inlet and outlet at the bottom of the tank (denoted as B-B). A tank that has a bottom inlet and top outlet (denoted as B-T) is shown in Figure 3.2(B) while in Figure 3.2(C) shows a configuration with the inlet at the top and the outlet at the bottom (denoted as T-B). A top inlet and top outlet configuration was not tested in this study, because it is rarely seen in practice arguably since such an arrangement cannot contribute to an increase in hydraulic disinfection efficiency. Moreover, CFD simulations were also performed for un-baffled bottom inlet bottom outlet and bottom inlet top outlet tanks with the same dimensions as those baffled tanks (see Figure 3.3). It is found from the result sections in this chapter that a small change in size of inlet/outlet will not affect the performance significantly, and thus un-baffled tanks were only tested with inlet and outlet of diameters of 2-in.

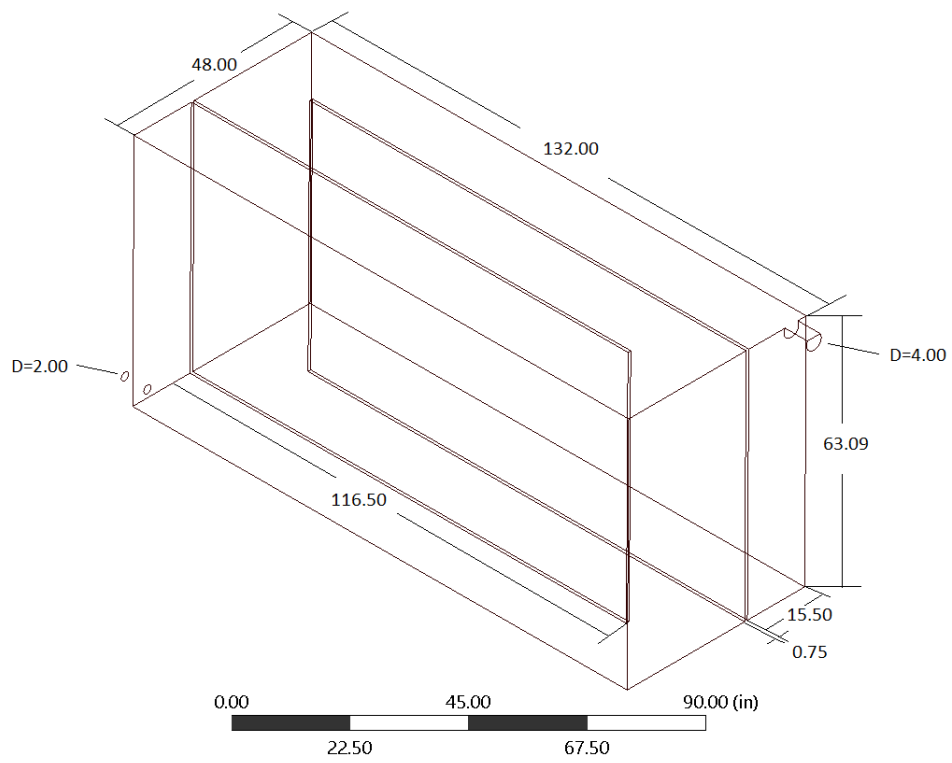
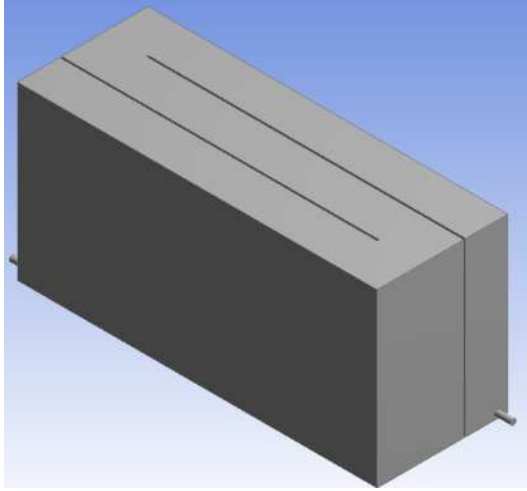
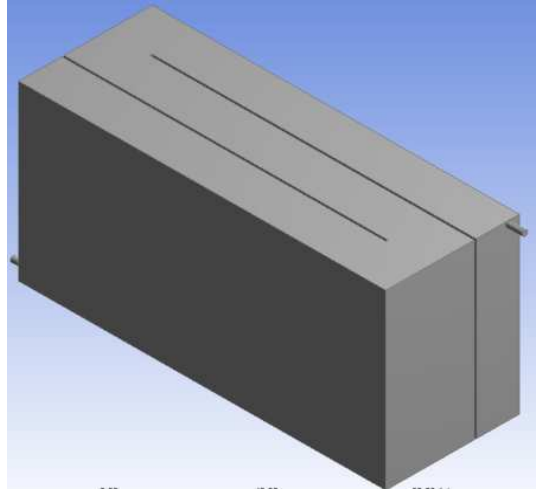


Figure 3. 1 Modeled geometry of a baffled contact tank and dimensions

A



B



C

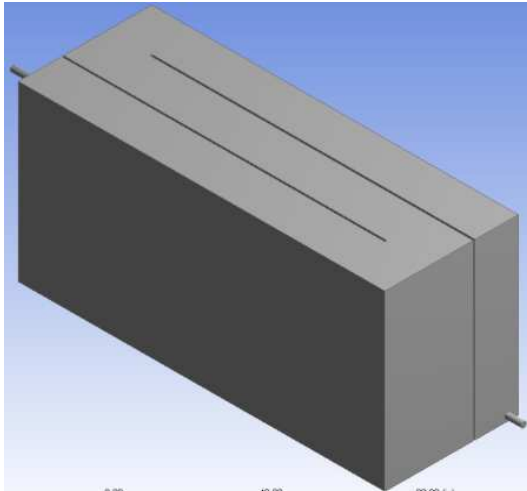


Figure 3. 2 Modeled geometry of baffled contact tanks. Bottom inlet and bottom outlet(A)
Bottom inlet and top outlet(B) Top inlet and bottom outlet(C)

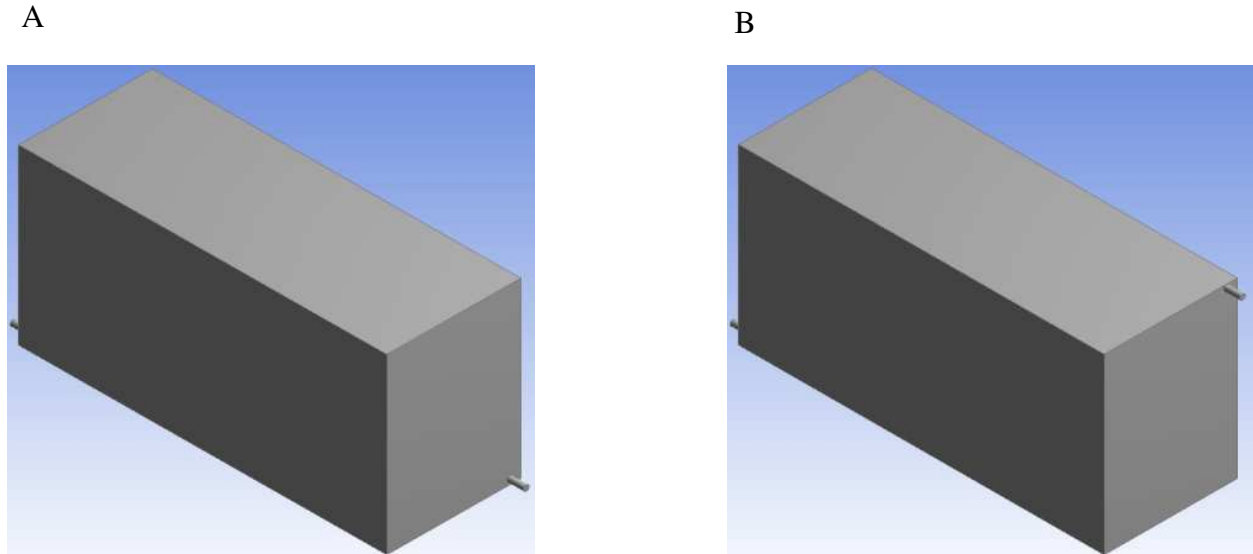


Figure 3. 3 Modeled geometry of un-baffled contact tanks. Bottom inlet and bottom outlet(A)
Bottom inlet and top outlet(B)

Physical tracer studies on the contact tank (as shown in the schematic in Figure 2.1) that is located in the Hydraulic Laboratory at CSU were conducted by previous investigators from this research group. Excellent agreements have been achieved between CFD results and physical tracer tests (see e.g. Katting 2014 & Carlston 2015). Considering the cost of rebuilding the tank by adjusting the location and size of the inlet/outlet, physical tracer tests were therefore not performed for the various inlet/outlet configurations in this study. Instead, CFD simulations were performed for these new configurations and the associated results will be discussed.

It has been addressed in chapter 2 that researchers should always be aware of the limitation due to errors when utilizing CFD simulations. Fortunately, by performing CFD simulations of a baffled tank with 2-in. bottom inlet and 4-in. top outlet, and comparing the results to several physical tracer tests conducted by Katting (2014) and Carlston (2015), excellent agreement between CFD results and tracer study results were obtained as shown in Figure 3.4. Hence, it is argued that the CFD simulations in this study have been reasonably validated to

justify new simulations to explore the variability of the configurations of the inlet/outlets as shown in Figures 3.2 (A-C).

In what follows, the numerical framework used in this study is briefly discussed. This is followed by results and discussion.

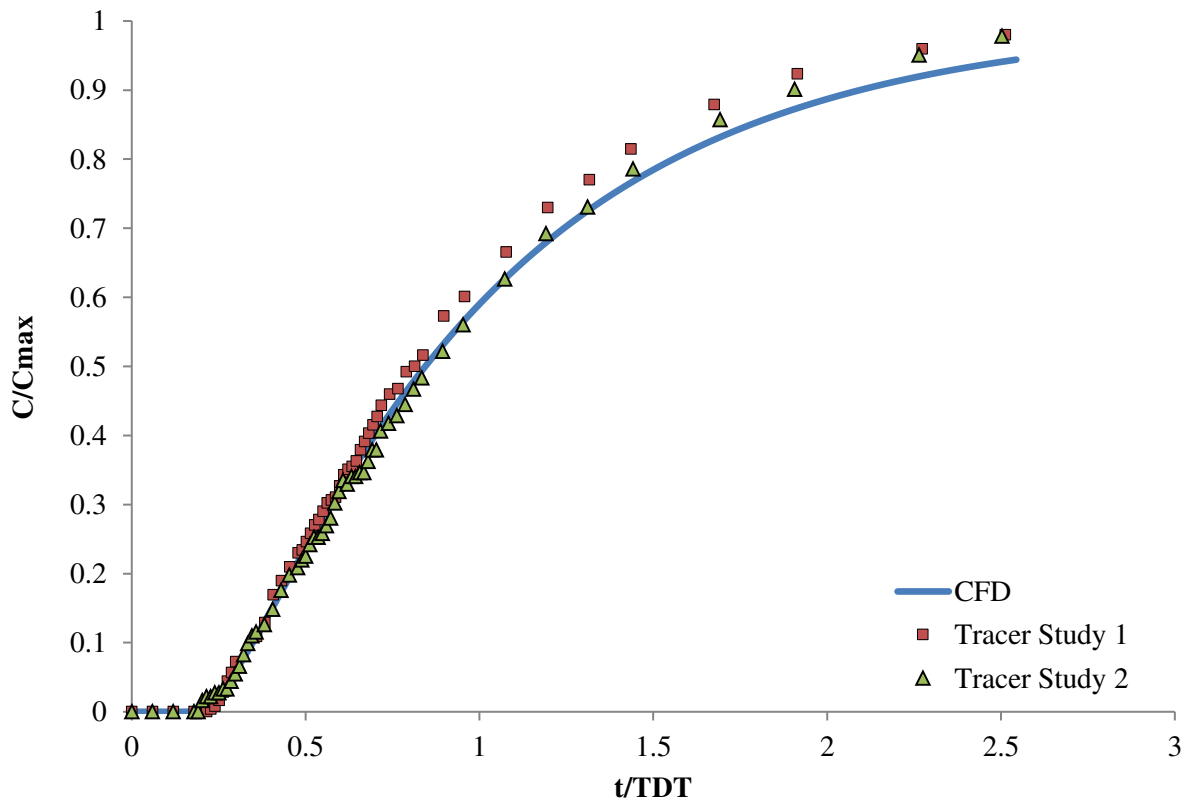


Figure 3. 4 Observed versus predicted cumulative RTDs at 40 gpm

3.3 Numerical Framework

3.3.1 Flow dynamics and scalar transport

It has been explained in chapter 2 that chemical and biological reaction processes were not considered to impact the hydraulic disinfection efficiency in the system due to the relatively short residence times of a tracer in the contact tank, and thus, the disinfectant (i.e. Chlorine) was treated as a passive scalar. Katting (2014) and Carlston (2015) utilized sodium-chloride and lithium-chloride as conservative tracers (i.e. passive scalars) for physical tracer tests, because

they do not react with water. Conductivities of tracers are then monitored at the outlet to obtain the residence time distribution (RTD) curves. Analogously, the transport of a passive scalar was modeled using CFD to obtain RTD curves. The transport of a conservative tracer was modeled using the advection-diffusion equation as follows

$$\frac{DC}{Dt} = \frac{\partial C}{\partial t} + \bar{U} \cdot \nabla C = \nabla \cdot ((\Gamma + \Gamma_t)C) \quad (3.1)$$

where C is the average tracer concentration. Here, $\frac{DC}{Dt}$ is the total time rate change of concentration and $\frac{\partial C}{\partial t}$ is the local time rate change of concentration; \bar{U} is the average steady state velocity; ∇C is the gradient of the average tracer concentration, Γ is the molecular diffusivity of the passive scalar, and Γ_t is the turbulent diffusivity of the passive scalar. It should be noted that the molecular diffusivity (Γ) is a characteristic of a given scalar diffusing in a given fluid medium while Γ_t is a flow property that can be calculated as $\frac{\nu_t}{Sc_t}$, wherein ν_t is the turbulent viscosity, and Sc_t is the turbulent Schmidt number. It has been discussed in chapter 2 that for neutrally stratified flows, the turbulent Schmidt number is approximately 0.7 (see e.g. Venayagamoorthy & Stretch 2010 for a justification).

3.3.2 Computational methodology

ANSYS Workbench version 16.2 was used to create tank geometries and meshes, and ANSYS FLUENT version 17.0 was able to perform the three-dimensional CFD simulations. Time-averaged flow fields were obtained by solving the Reynolds averaged Navier-Stokes (RANS) equations using the Re-normalization group (RNG) $\kappa - \varepsilon$ turbulence model. The $\kappa - \varepsilon$ model includes two-equation turbulence model which allows the determination of time and length scales by solving two separate partial differential (transport) equations. Compared to the standard $\kappa - \varepsilon$ model, the RNG $\kappa - \varepsilon$ model is able to improve the accuracy for swirling and

rapidly strained flows which are very likely to occur near the inlet jet in the tank. The RNG $\kappa - \varepsilon$ model has been shown to be more accurate for low-Reynolds number flows that are typical close to solid boundaries (ANSYS, 2013). Moreover, to achieve more accurate results, enhanced wall functions were used. Computational models were initialized with velocity-inlet and pressure-outlet options with a specified turbulent kinetic energy, κ , turbulent kinetic energy dissipation rate, ε , prescribed inlet velocity, and zero gauge pressure at outlet. No-slip boundary condition was applied on all tank walls. In order to avoid multi-phases in the flow model, the free-surface was treated as a wall without shear stress (i.e. a symmetry boundary condition was thus applied). The simulation was conducted in two steps. First, the mean velocity field (i.e. \bar{U}) and turbulent viscosity, ν_t were computed for steady-state conditions. Then the simulation was restarted under transient conditions to compute the scalar transport by utilizing the converged velocity fields obtained from the first step. The scalar was introduced at inlet, and a monitor was turned on at the outlet to report area-weighted averaged scalar concentration at each time step. These results were obtained using equation (3.1) and a residence time distribution (RTD) curve for the scalar at the outlet can thus be obtained. In order to non-dimensionalize the computed RTD curve, the concentration at the outlet was normalized by the maximum concentration of the scalar in the tank and time was normalized by the theoretical detention time (TDT) which varies with flow rate. Figure 3.6 shows the RTD curves for all baffled tank simulations that were performed for this study.

A mesh independence study which includes assessment of the adequacy of spatial resolution and temporal resolution was performed on the modeled tank by Kattnig (2014) to ensure convergence of numerical results as well as optimality in terms of computational costs. It had been found that for this study that the 3-D baffled tank with meshes finer than 1 million cells

yield converged results i.e. the results are mesh independent as shown in Figure 3.5A. Similarly, a temporal resolution study also showed that coarsening the time step Δt had no significant effect on t_{10} , or on the shape of the RTD curve and only mildly affected later portions of resulting curves. A final time step of 5s was selected for all simulations. A mesh consisting of 1.4 million cells was used for all simulations. Moreover, most models were run at three different flow rates (i.e. 10 gpm, 20 gpm, and 40 gpm) with identical simulation configurations in order to explore the effects of flow rate on baffling factors.

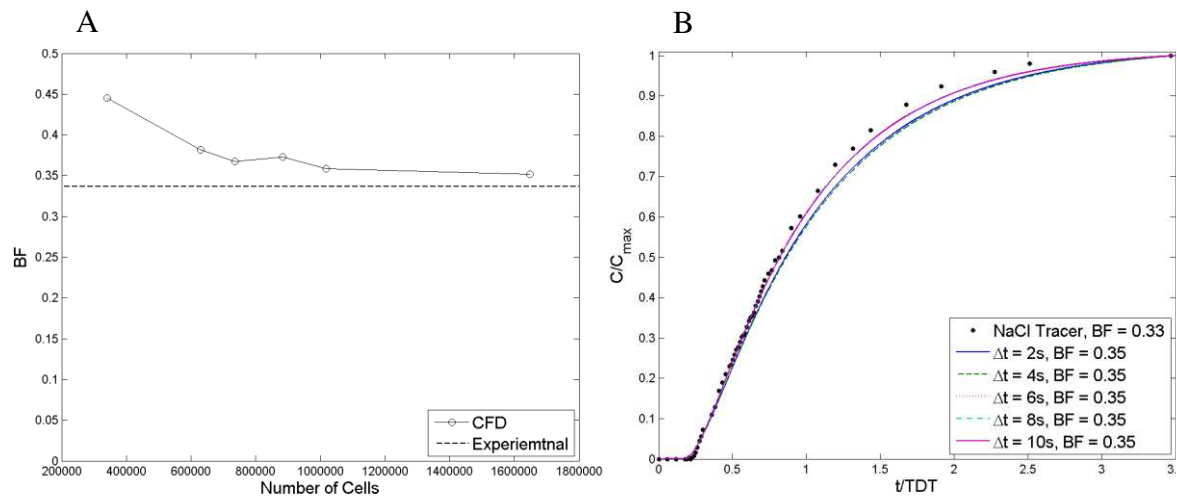


Figure 3. 5 Mesh independence study of spatial solution (A) and temporal solution (B)

3.4 Results

3.4.1 Baffled tanks

Clearly, residence time distribution (RTD) is a good way to estimate the hydraulic disinfection efficiency by showing the overall process of disinfection graphically. On the other hand, quantification of the hydraulic disinfection efficiency is more convenient to evaluate a disinfection system. Thus, the baffling factor (BF) is used to quantify the hydraulic disinfection efficiency.

Resulting RTD and associated BF for all the configurations explored for baffled tanks are shown in Figures 3.6-3.8 & Table 3.1. The BFs varied from 0.29 to 0.4. In order to investigate the effect of outlet size on hydraulic disinfection efficiency, a bottom inlet-top outlet tank with outlet size of 2-in.-diameter and 4-in.-diameter were simulated at 20 gpm. The corresponding RTD and BF do not show significant differences compared to the 2-in diameter inlet/outlet configuration at 20 gpm,. This indicates that the modification of inlet/outlet size does not affect the hydraulic disinfection efficiency significantly. The reason can be the modification on inlet/outlet dimension is relatively small compared to the entire tank dimensions. Hence, all other simulations henceforth were done using only 2-in.-diameter outlets. Considering flow rate could affect the hydraulic disinfection efficiency due to turbulence, RTD curves and BFs for different flow rates (i.e. 10 gpm, 20 gpm, and 40 gpm) are shown separately in Figures 3.7 (A), (B), and (C) to eliminate the dependence on flow rate. It is found that RTD curve varies significantly between the three inlet-outlet location configurations regardless of the flow rate. Table 3.1 summarizes the BF for each configuration tested at various flow rates and is sorted from lowest to highest BF. It can be seen that the bottom inlet and bottom (B-B) outlet, which is the most common case found in practice, performs the worst (BF = 0.29); while the top inlet-bottom outlet (T-B) configuration performs the best (BF = 0.4). From the worst case to the best case, the baffling factor ranged from 0.3 to 0.4, indicating that different configurations of the inlet/outlet location can result in gains in baffling factor in excess of 30% for a baffled contact tank. As mentioned above, the change in flow rate could impact the BF due to turbulence. Figure 3.8 shows the effect of flow rate on hydraulic disinfection efficiency for the top inlet bottom outlet (T-B) tank. Given the same tank configuration, the system performed similarly at various flow rates. The BF increased from 0.39 to 0.43 with flow rate increasing from 10gpm to 40gpm. The

reason for this increase in BF could be due to more effective mixing at higher flow rates. In summary, the effects of inlet and outlet locations on the hydraulic disinfection efficiency of baffled contact tank can be significant, especially at low flow rates.

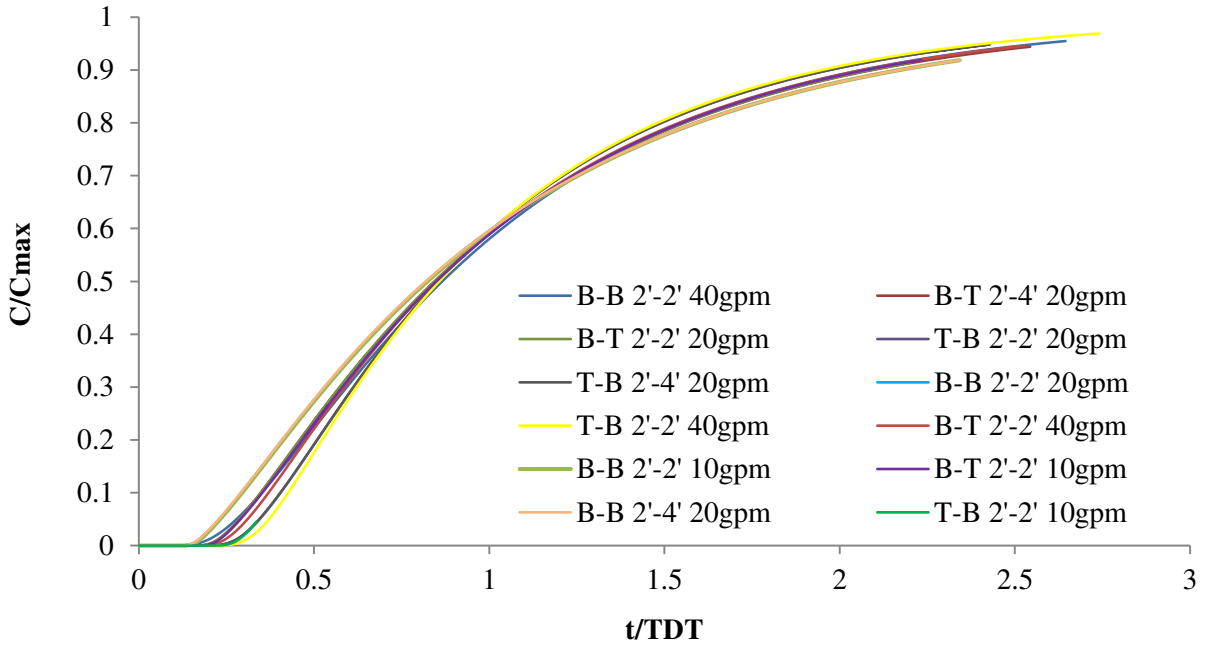


Figure 3. 6 RTD curves for all CFD simulations of baffled tanks (see Table 3.1).

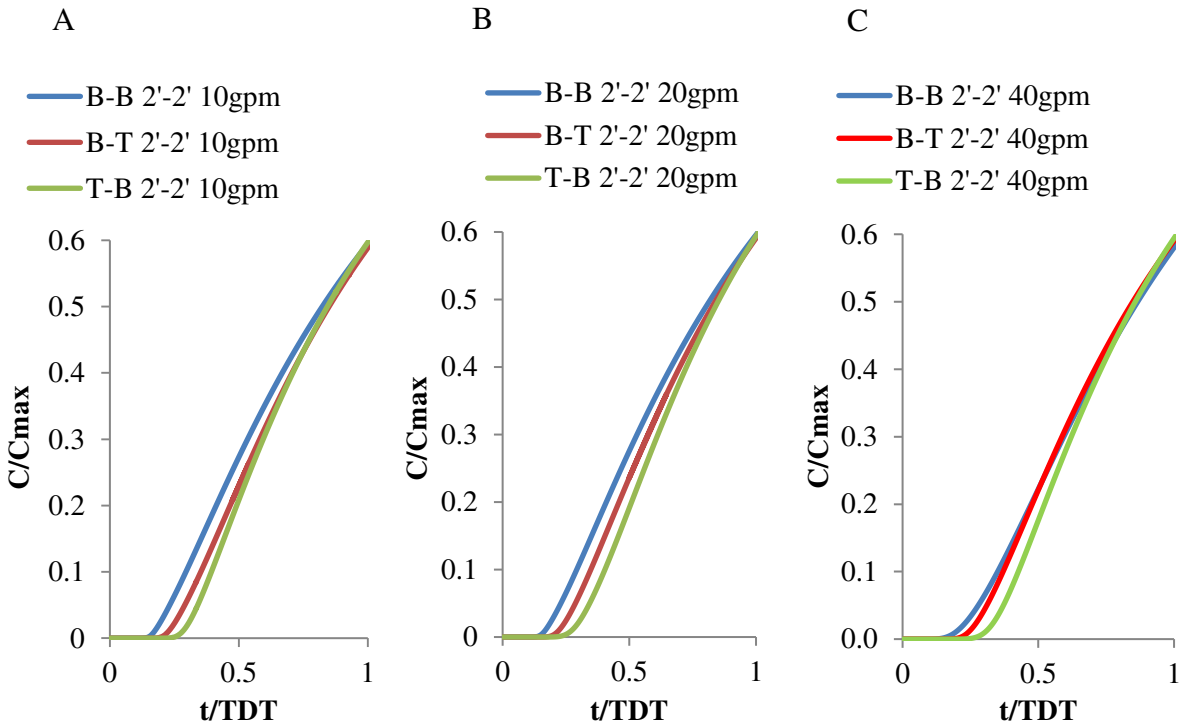


Figure 3. 7 RTD curves for each 2-in. diameter inlet/outlet location modification at (A) 10gpm (B) 20gpm (C) 40gpm

Table 3. 1 Baffling factors for all configurations

10gpm	BF	20gpm	BF	40gpm	BF
B-B 2'-2'	0.29	B-B 2'-2'	0.29	B-B 2'-2'	0.35
B-T 2'-2'	0.35	B-B 2'-4'	0.29	B-T 2'-2'	0.37
T-B 2'-2'	0.39	B-T 2'-2'	0.35	T-B 2'-2'	0.43
		B-T 2'-4'	0.35		
		T-B 2'-2'	0.4		
		T-B 2'-4'	0.4		

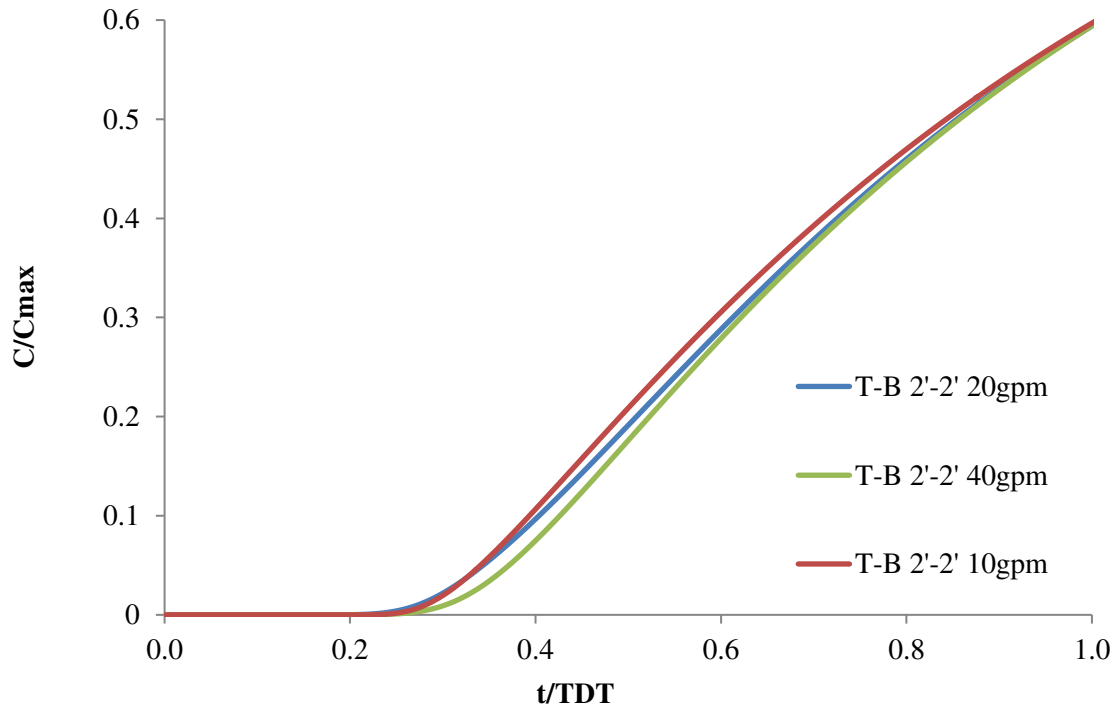


Figure 3. 8 RTD curves for 2-in. diameter T-B configuration at various flowrates

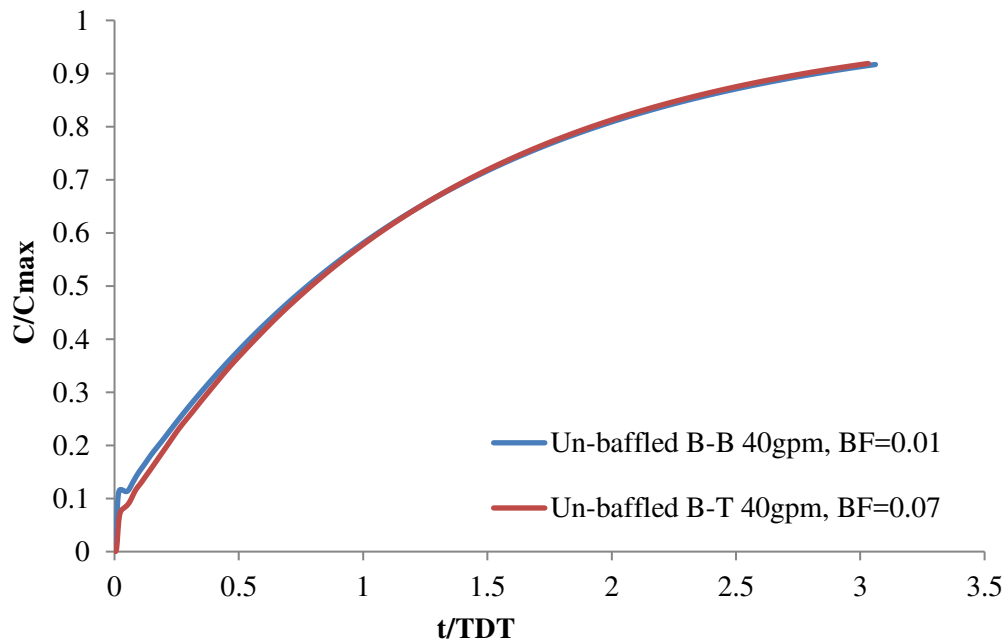


Figure 3. 9 RTD curves for un-baffled tanks at 40gpm

3.4.2 Un-baffled tanks

To make this study more comprehensive, tanks without baffles were also studied to investigate the effect of inlet/outlet location on baffling factors. Figure 3.9 shows the RTD curves for the bottom inlet bottom outlet and top inlet bottom outlet tanks (See Figure 3.3 for tank geometry). For a bottom inlet bottom outlet un-baffled tank, the baffling factor could be as low as 0.01, while if the outlet were placed to the top, the BF went up to 0.07. It is also found that the influence of inlet/outlet location was more conspicuous at the beginning of the process on the rising limb of the RTD. Figure 3.9 shows that the two curves converge towards the later stages. Although a modification on outlet location increased the baffling factor by as much as seven times, BF for both cases was lower than 0.1, which is defined as a highly inefficient system (USEPA 2003). Hence, the baffling factors for the un-baffled tank were too low (< 0.1) to give satisfactory disinfection performance from simple reconfiguration of the location of inlet/outlet.

3.5 Discussion

3.5.1 Velocity magnitude analysis

The results of the baffled tank simulations show that the inlet/outlet location does influence the hydraulic disinfection efficiency of baffled tanks by as much as 30%. In order to study how the inlet/outlet location affects the hydraulic disinfection efficiency for baffled tanks, hydrodynamic analysis was conducted. It should be noted that the inlets and outlets are located at diagonally opposite ends of the tank in order to ensure that the flow has the longest path through the tank. All the location modifications are in vertical direction in which the gravity plays an important role. In order to understand the flow field in the tank for any given inlet/outlet configuration, the overall velocity magnitude and the vertical velocity magnitude of the 2-in.-

diameter inlet/outlet tank with various inlet/outlet locations at 20 gpm were extracted from the simulations and given in Table 3.2. The velocities were measured at two specific levels, i.e. at 2-in. and 62-in. above tank floor. All velocity magnitudes are in m/s. The 2-in. level is a plane that intersects the center of the bottom inlet/outlet, while the 62-in. level intersects the center of the top inlet/outlet. The mean velocity was averaged over the entire tank volume, and the velocities at a specific level are area-weighted average values. Negative sign indicates downward direction for the vertical (y) velocity.

Table 3. 2 Velocity magnitude (m/s) for 2-in. diameter inlet/outlet tanks with various inlet/outlet locations at 20 gpm

	Mean		y=2in.		y=62in.	
	y velocity	velocity	y velocity	velocity	y velocity	velocity
B-B	-3.1e-6	0.013	-3.2e-5	0.044	8.0e-6	0.023
B-T	2.8e-4	0.016	6.4e-5	0.042	1.3e-4	0.026
T-B	-2.9e-4	0.015	-5.7e-5	0.021	-2.9e-4	0.041

It can be seen in Table 3.2 that the overall velocity magnitude does not vary much among the three configurations, yet the vertical velocity varies by two orders of magnitude among the three configurations. For each configuration, the highest mean velocity occurred where the center of the inlet is located. For example, the mean velocity magnitude of bottom inlet bottom outlet tank at y=2in. was 0.044m/s that was greater than the volume weighted averaged velocity and that was also greater than the velocity at y=62in.. Hence, the flow would be more turbulent around inlet region. Besides, for the volume-weighted average and the area-weighted average at y=62in., the bottom inlet bottom outlet tank had a vertical velocity that is of the order of 1e-6 m/s while the other two had a vertical velocity in an order of 1e-4 m/s. The much lower y-velocity within the bottom inlet bottom outlet tank, especially at the upper part of the tank, indicates a dead zone must have occurred at the upper portion of the fluid. The magnitudes of vertical

velocities were very close at $y=2\text{in.}$, due to the momentum introduced by influent and the wall effect coming from the tank floor.

3.5.2 Magnitudes of flow velocities

Figure 3.10, Figure 3.11, and Figure 3.12 depict flow velocity contours at various levels. Color indicates velocity values in the domain. The largest velocity magnitudes are shown in red, while the smallest are shown in blue. Note that color scale is not comparable among different figures due to different velocity magnitudes. For vertical velocity, negative value indicates downwards direction. For overall velocity contour, zero was the smallest velocity magnitude, demonstrating stagnation region.

Figure 3.10 and Figure 3.11 show a y -velocity distribution for bottom inlet bottom outlet configuration (A), bottom inlet top outlet configuration (B), and top inlet bottom outlet configuration (C) at $y=2\text{in.}$ and $y=62\text{in.}$ respectively. All figures show a visible separation around the first baffle turn opening, resulting from an upward momentum generated by the back wall. For the two bottom inlet tanks, the flow jet created by the inlet hit the back wall of the tank at the bottom, and thus more fluid moved upwards and created a counter-clockwise circulation near the back wall. This upward momentum is opposite to gravity and could be suppressed. The bottom inlet-bottom outlet configuration performed worst because the bottom outlet encouraged the influent water to stay at the bottom, generating a short circuiting near the tank floor, and left a dead zone at the upper portion of the flow. On the other hand, the top inlet bottom outlet configuration created a clockwise circulation in the first channel, so the injected forward momentum could help to overcome the dead zone that may occur at the top and the downwards momentum near the first turn opening could also be encouraged by gravity. Thus, the influent would be mixed more efficiently with the ambient storage water.

Figure 3.12 gives the overall velocity contour at a plane that intersects the center of the inlet. There is no noticeable difference in this figure since longitudinal velocity dominates at this level. As indicated in Table 3.2, the plane intersecting the center of the inlet should be most active, but a large area of dead zones colored in dark blue occurred in the second and third channels, especially for the two bottom inlet configurations. Hence, this suggests that a proper modification on inlet/outlet location, such as displacing the inlet to the top and the outlet to the bottom, will result in higher hydraulic disinfection efficiency. In summary, the inlet/outlet location could affect hydraulic disinfection efficiency significantly.

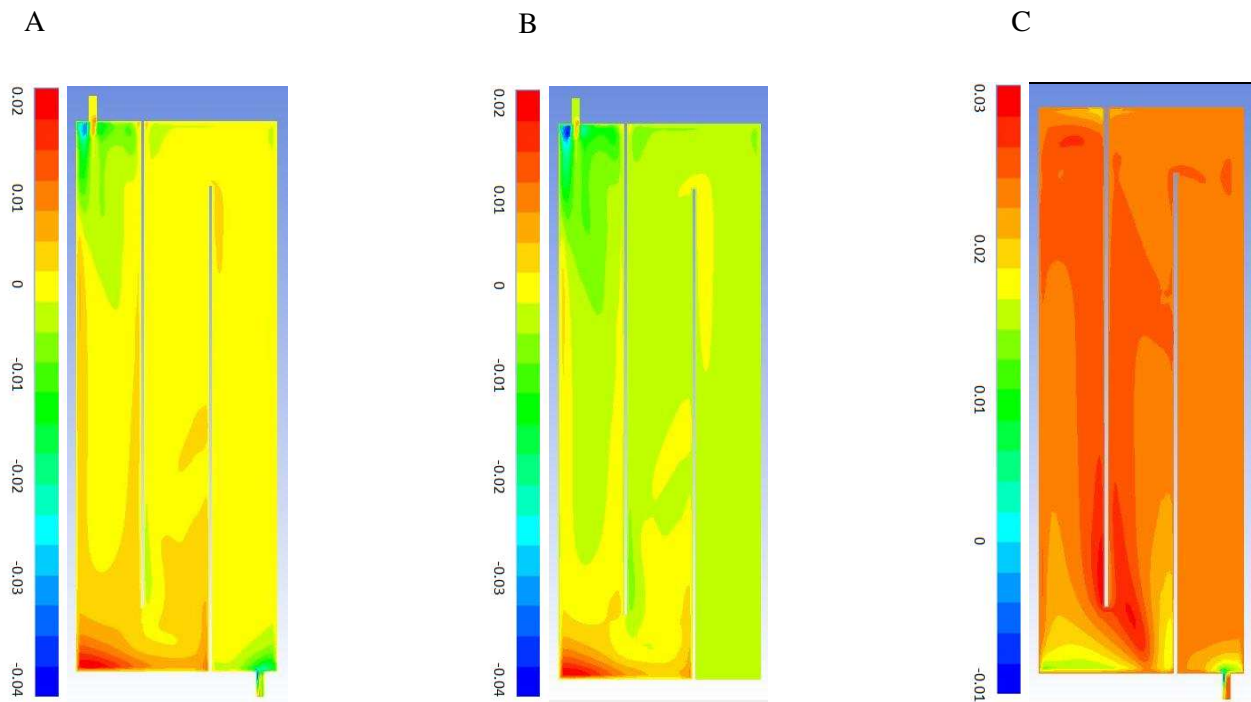


Figure 3. 10 Vertical velocity field for 2-in.-diameter inlet/outlet tanks at $y=2\text{in.}$ for B-B (A) B-T (B) and T-B (C)

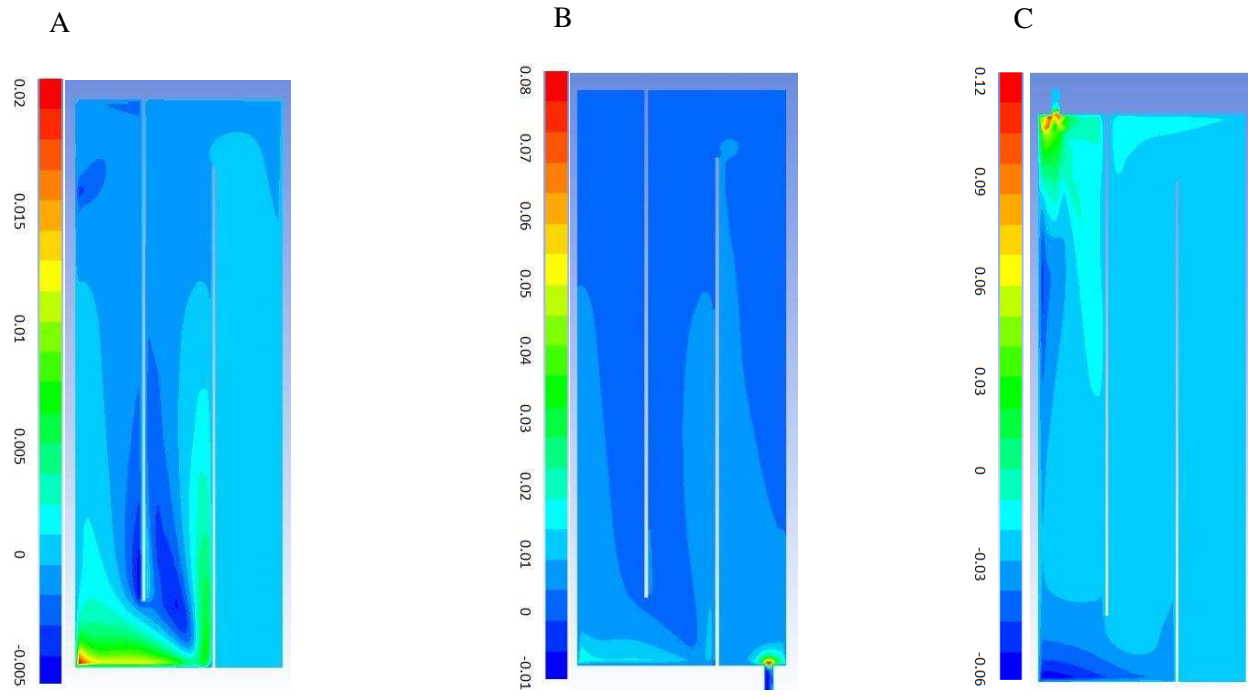


Figure 3. 11 Vertical velocity field for 2-in.-diameter inlet/outlet tanks at $y=62$ in. for B-B (A) B-T (B) and T-B (C)

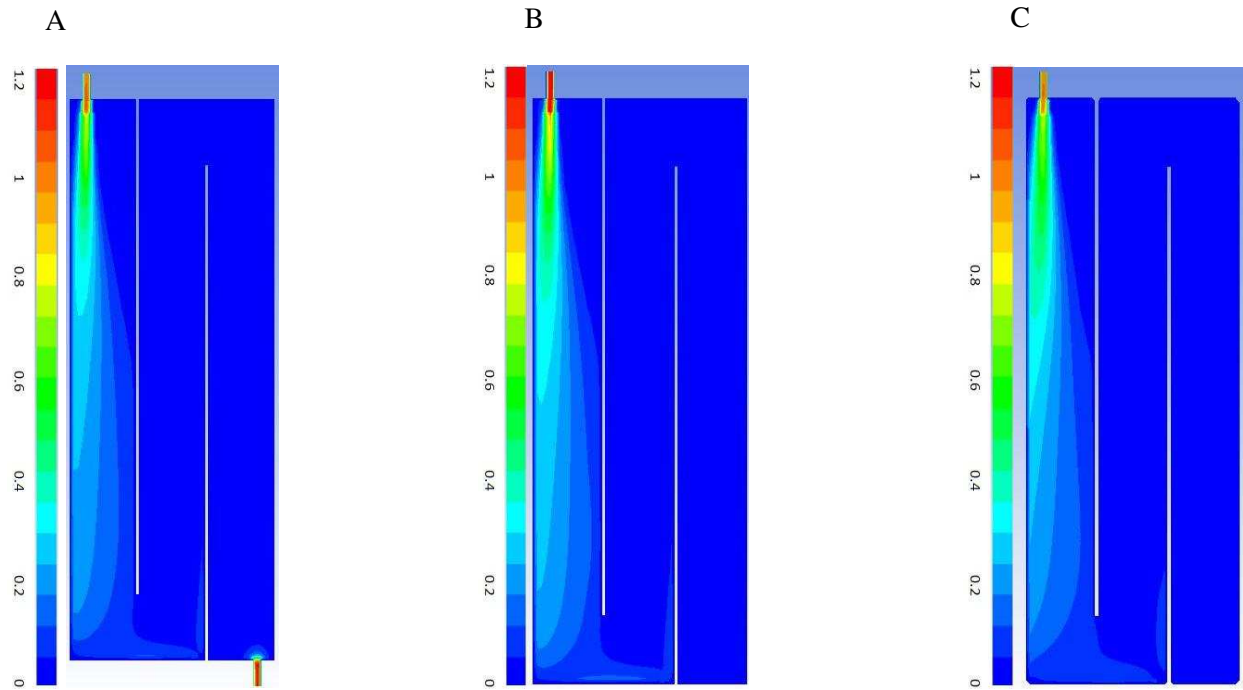


Figure 3. 12 Overall velocity at inlet plane for B-B (A) B-T (B) and T-B (C)

3.6 Conclusion

This study focused on investigating the effects of inlet/outlet location and size on baffling factor and hydraulic disinfection efficiency. By comparing the baffling factors for various inlet/outlet locations and sizes, it was found that the baffled tank performed much better than unbaffled tanks. For baffled tanks, the configuration with the top inlet and bottom outlet resulted in higher performance (over 30%) compared to the configuration with the bottom inlet and bottom outlet commonly found in practice. A small modification of the inlet location results in a considerable increase in the hydraulic disinfection efficiency. On the other hand, small modifications to the inlet/outlet sizes did not affect significantly affect hydraulic disinfection efficiency.

CHAPTER 4 BUOYANCY EFFECTS

4.1 Introduction

As discussed in chapter 3, the location of the inlet/outlet does influence the hydraulic disinfection efficiency significantly in neutral flows. Due to the presence of more dead zones and short-circuiting, the bottom inlet-bottom outlet configuration gives the worst performance. On the other hand, the top inlet-bottom outlet configuration had a hydraulic disinfection efficiency that was 30% higher than the bottom inlet-bottom outlet configuration. However, neutral flow conditions are not always possible. In fact stratified flow conditions occur in environmental and geophysical applications. For example, in the ocean, stratified turbulence mediates the mixing and transport of water masses, nutrients, and chemicals. In the atmosphere, stratification affects the transport of pollutants released at ground level. In building ventilation, the circulation of air and heat are controlled by ambient stratification. Specifically in relation to the current study in industrial hydraulic applications, stratified flows could occur in numerous units of drinking water treatment plants. A disinfection contact tank is an example that is predominantly subjected to stratification. Hence, the turbulence in the system might be either suppressed or enhanced by the stratification. The above-mentioned examples show that stratification is of board interest in many environmental, industrial, and geophysical flows. Hence, it is important to investigate how density variations impact the hydrodynamics in a contactor and how different the hydraulic disinfection efficiency compared to the case of neutral flows (see Chapter 3).

In this chapter, both baffling factor and Morrill index will be utilized to quantify the hydraulic disinfection efficiency of the disinfection tank. It should be noted that BF provides a

measure of the short-circuiting in the tank, while MI provides a measure of the dispersion. These two indicators together provide a better picture of the hydraulic disinfection efficiency.

4.2 Description and Motivation behind Buoyancy Effect

Buoyancy effects are important in a disinfection system when the temperature and/or concentration of inflow are different from the ambient water in the tank. As alluded to previously, the colder the water is and the higher concentration of sediments and other matter in the water, the denser the water would be. Such incoming water can result in the generation of density currents in the tank. In such cases, the flow tends to depart further away from plug flow conditions due to vertical motions, especially in pipe systems. Goula et al. (2008) focused on the density current in primary sedimentation tank for drinking water treatment. In their study, the temperature variation is the main reason for density differences. Besides the study of Goula et al. (2008), other studies (TeKippe & Cleasby, 1968; Wells & LaLiberte, 1998; Amir & Schroeder, 1999; Taebi-Harandy & Schroeder, 2000) showed that the difference between tank temperature and the influent temperature could impact the flow pattern in a given system. A strong correlation between the hydrodynamics and temperature gradient in the system is expected and a small temperature difference such as 1°C or 0.2°C seemed large enough to induce a density current. Most of the previous studies on drinking water treatment units were performed on clarifiers. Only a handful of studies have focused on disinfection tanks with hardly any detailed application of CFD models to address this issue in disinfection systems. This chapter thus aims to provide some insights of the effect of buoyancy in disinfection tanks. Even though insufficiently mixed inflow could result in a variation in concentration, leading to a variation in density; for the purpose of this study, temperature is assumed to be the only factor that affects the density of the water.

Temperature variation is common in practical disinfection tanks and it could change seasonally. Some disinfection tanks are placed indoor, where the water temperature inside is relatively constant compared to inflow from the supply line. In winter, the influent temperature is lower than the storage water, generating a negatively buoyant force. New inflowing water tends to stay at the bottom due to its high density. On the other hand, in summer, the influent temperature is higher than the storage water and the inflow would rise to the top layers in the tank due to its lower density. Therefore, the flow paths inside a disinfection tank are likely to change seasonally because of density variations, resulting in a change in hydraulic disinfection efficiency. Unfortunately, this phenomenon is often overlooked. The main objective of this study is to provide insights into the fluid mechanics of stratified flows in a disinfection system with particular emphasis on hydraulic disinfection efficiency.

4.3 Methodology

Considering the difficulty in temperature control and time consumption, only computational simulations were conducted for this study research. Fortunately, Kattning (2014) and Carlston (2015) have performed physical tracer tests on the disinfection tank (that was discussed in chapter 3) with uniform temperature distribution. As shown in Figure 3.4, remarkable agreement between RTD curves from tracer studies and CFD were obtained.

4.3.1 Geometry description

The benchmark computational model in this study was modeled based on the disinfection tank that is located at the Hydraulics Lab at Colorado State University, (Figure 4.1). A plan-view of the geometry of the baffled contact tank is depicted in Figure 4.2. All dimensions are in inches.

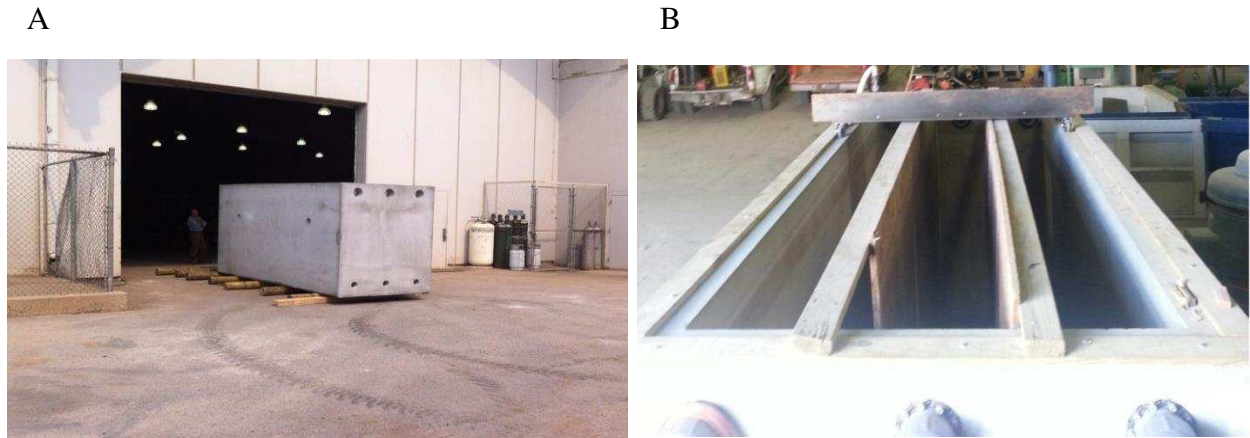


Figure 4. 1 1500-gal physical prototype (A) Geometric plan view of baffled system prototype (B)

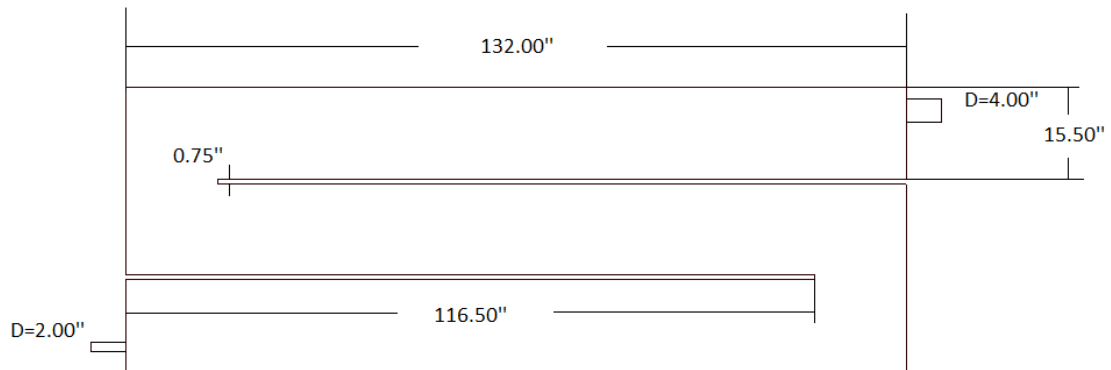


Figure 4. 2 A schematic plan view of the baffled tank used in this study

The base geometry was built with bottom inlet and top outlet. Six flowrates (i.e. 10gpm, 20gpm, 30gpm, 40gpm, 50gpm, and 60gpm) were simulated for this configuration under two scenarios for generating temperature differences. Furthermore, a top inlet-bottom outlet configuration was also simulated at flow rates of 20gpm and 40gpm, given its superior performance (as discussed in chapter 3) in neutral flows.

4.3.2 Scenario description

As mentioned previously, the indoor water has a relative constant temperature compared to the influent fluid from outdoors. In winter, an influent jet with a low temperature is likely to be introduced into the tank. In order to simulate this, an initial temperature was set to room temperature (i.e. 20°C) for the fluid in tank, and then the temperature of the inlet jet was set to three different values, 5°C, 10°C, and 15°C, respectively. Note the previous results from chapter 3 could therefore be considered equivalent to the case in which inlet jet temperature is 20°C. The temperature difference from 5°C to 15°C with a 5°C increment was then generated. Two scenarios were modeled for this temperature differences. The first scenario is where a no heat flux condition was enforced between the fluid and the walls. The second scenario maintains the temperature of walls as a constant (i.e. at 20°C). Both scenarios were modeled with various influent temperatures and flow rates. The RTD curve of each scenario and the corresponding BF with respect to temperature difference and flow rate curves are presented in the results section.

4.3.2.1 No heat flux

A total number of five flow rates (i.e. 10gpm, 20gpm, 30gpm, 40gpm, and 50gpm) were simulated under the assumption that there was no heat exchange between the fluid and walls. In this scenario, no extra heat source is added to the system, while a cold influent is continuously injected. Thus, the temperature distribution in the tank would change transiently until the tank temperature reduces to the influent temperature at steady state.

4.3.2.2 Constant wall temperature

All walls including outside walls and baffle walls were kept at a constant temperature and hence serve as a heat source. Initially, all walls and the storage water were kept at room temperature (i.e. 20°C), and then cold influent was injected with 5°C. Because of the constant

heat source from the walls and a steady stream of cold influent, the temperature distribution, or flow stratification was maintained even at large times (i.e. when the steady state conditions were achieved). A constant wall temperature condition might occur when the surrounding are much warmer than the influent, so that the cold inlet flow would hardly affect the wall temperature. This condition is not as common as scenario 1, but it is still valuable to access such a situation and compare it to scenario 1.

4.3.3 Numerical model

4.3.3.1 Governing Equations

In addition to the continuity equation and Navier-Stoke's equation, the energy equation (Equation 4.1) was also used to simulate the effects of temperature differences in this chapter.

$$\rho_o \frac{\partial}{\partial t}(E) + \nabla \cdot (\vec{U}(\rho_o E + P)) = \nabla \cdot \left((\Gamma + \Gamma_t) \nabla T - \sum_j h_j \vec{J}_j + \mu \nabla \vec{U} \cdot \vec{U} \right) \quad (4.1)$$

Equation 4.1 was explained in detail in chapter 2. Stemming from the first law of thermodynamics, a dynamical equation for the internal energy, e , is shown in Equation 4.2.

$$\frac{De}{Dt} = Q - p \frac{Dv}{Dt} \quad (4.2)$$

Where v is the unit mass of volume and Q is the heat added due to diffusion process. For any constant volume transformation, the internal energy e is equal to $C_v T$ where C_v is the heat capacity per unit mass. Equation (4.2) thus becomes Equation (4.3).

$$C_v \frac{DT}{Dt} = Q - \frac{p}{\rho^2} \frac{D\rho}{Dt} \quad (4.3)$$

Under the assumption that water is incompressible, water density does not change with pressure, and thus density fluctuations exclusively arise from the change of temperature and salinity. For

the purpose of this study, temperature was considered as the only factor that could change the water density. Hence, a linear equation of state may be expressed as Equation (4.4).

$$\rho = \rho_o[1 - \alpha(T - T_o)] \quad (4.4)$$

According to physical property of water table (Munson et al., 2009), the water density was assigned previously by piecewise-linear model in FLUENT. Water density at five points were defined, such as at the temperature of 0°C, 5°C, 10°C, 20°C, and 30°C. Interpolation would be performed when the local temperature is not on these nodes. According to Fourier Law: $\rho Q = \kappa \nabla^2 T$ (κ is the material's conductivity), Q could be rewritten as $\frac{\kappa \nabla^2 T}{\rho}$, and based on Boussinesq approximation $\frac{D\rho}{Dt}$ is negligible. One could easily get Equation (4.5)

$$\frac{DT}{Dt} \propto \nabla^2 T \quad (4.5)$$

Finally, the temperature of the incoming water could be treated as a scalar as showed in Equation (4.5). The value of the influent temperature is incorporated in the tank and is then transported using an advection-diffusion partial differential equation (Equation 4.6).

$$\frac{DT}{Dt} = \frac{\partial T}{\partial t} + \bar{U} \cdot \nabla T = \nabla \cdot ((\Gamma + \Gamma_t) \nabla T) \quad (4.6)$$

By solving the above equations, the temperature distribution changes over domain due to a cold influent, resulting in the change of density distribution.

The Boussinesq approximation could be applied in this chapter to simplify the equations because the associated assumptions were satisfied in this study. First, the influent temperature increased from 5°C to 20°C, and the corresponding density could decrease from 1000kg/m³ to 998.2kg/m³ (Munson et al., 2009). This density difference ($\Delta\rho= 1.8\text{kg/m}^3$) is small compared to water density at 20°C (i.e. 998.2kg/m³). Moreover, the inertial acceleration for the water in the

tank is small compared to the gravitational acceleration, as the water viscosity is relatively small (i.e. in the order of $1\text{E-}6 \text{ m}^2/\text{s}$).

In the momentum equation (Navier-Stokes equation), ρ comes into play in two terms, one is the temporal acceleration, $\frac{\partial}{\partial t}(\rho\vec{U})$ and the convective acceleration, $\nabla(\rho\vec{U} \cdot \vec{U})$; the other is gravity term, $g\rho$. As stated in Boussinesq approximation, ρ could be replaced by ρ_o in the acceleration terms, but the bulk density cannot be replaced in the later gravitational term. This is why a modified acceleration, $\frac{\rho'}{\rho_o}\vec{g}$ results in the Boussinesq approximation form of the Navier-Stokes equation.

4.3.3.2 Schmidt number

As mentioned in chapter 2, the turbulent Schmidt number was used to calculate turbulent diffusivity coefficient. However, the determination of this Schmidt number is controversial, especially for stratified flows. Many studies (Flesh 2002; Venayagamoorthy and Stretch 2010; Yimer et al., 2002; Yoshihide & Stathopoulos 2007) indicate that a value of Schmidt number ranging from 0.5 to 0.9 was widely accepted in CFD simulations for fluid flows. This study thus applied 0.5, 0.7, and 0.9 as Schmidt number to the selected models. Figure 4.3 and 4.4 illustrate the RTD curves from simulations at 40gpm under no heat flux condition and constant wall condition, respectively.

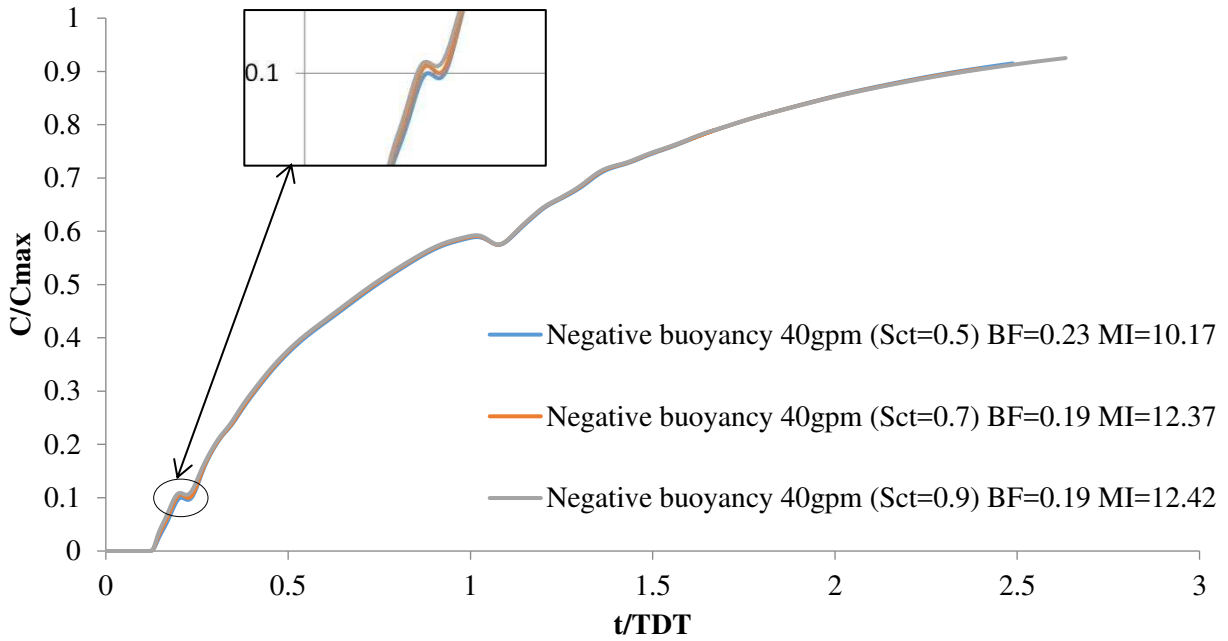


Figure 4. 3 RTD curve for no heat flux condition at 40gpm with turbulent Schmidt numbers of 0.5, 0.7, and 0.9.

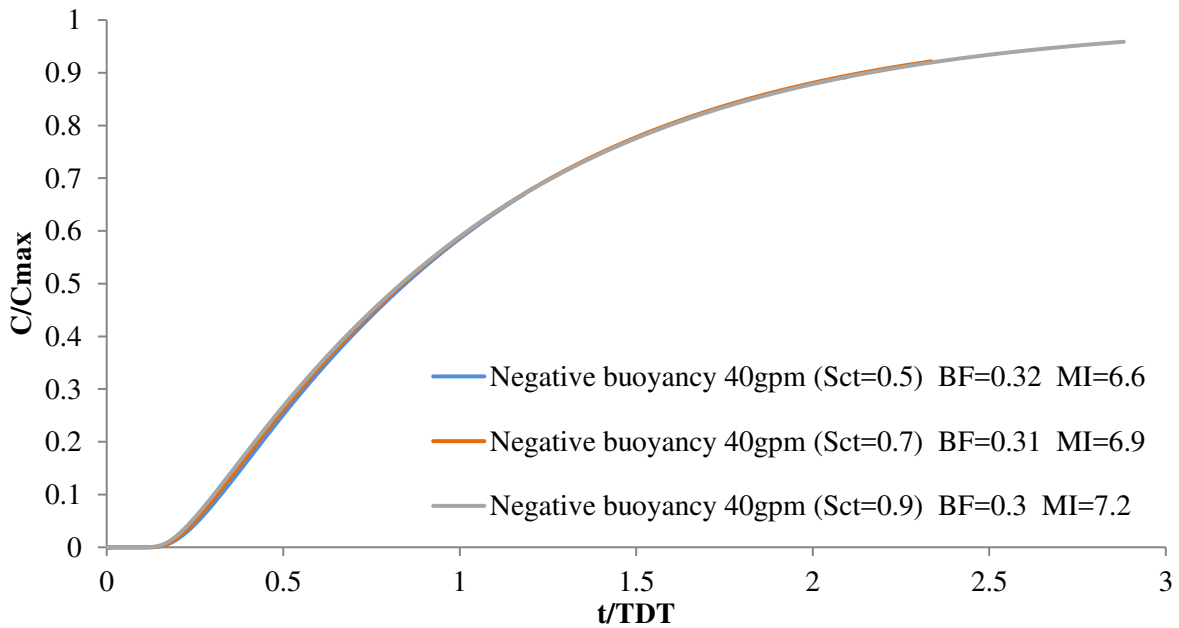


Figure 4. 4 RTD curve for constant wall temperature condition at 40gpm with Schmidt number of 0.5, 0.7, and 0.9

It can be seen from Figures 4.3 and 4.4 that the three curves with various Schmidt numbers are very close to each other. However, compared to constant wall temperature condition, the baffling factors and Morrill indices for the no heat flux condition were more sensitive to changes in Schmidt number. The reason could be due to the fluctuation that occurs around $C/C_{\max}=0.1$ as the temperature distribution changes. However, the general trend for all three cases with various Schmidt numbers is similar. Based on these findings, the widely accepted value of 0.7 was used hereafter.

4.4 Results and Discussion

Results from neutral flows simulations showed that a BF of about 0.35 for the bottom inlet-top outlet configuration (see chapter 3 for details). This result is attributed to the fact to the large dead zones and short-circuiting that occurs in the tank. For the case where a dense influent is introduced into the tank, it was initially expected for this jet to propagate along the bottom of the tank and then rise to the outlet once it hits the back wall. Thus, as a result, it is expect that the residence time of the influent will be increased and thus a higher BF would be obtained. However, it turns out that the results to be discussed reveal a more complex problem when buoyancy is included.

4.4.1. RTD curves for 5°C influent temperature

The results for both scenarios will be discussed using RTD curves, BF-Q (flow rate) curves, and BF- ΔT (temperature difference) curves. The buoyancy affected results are also compared to those obtained under uniform temperature condition.

4.4.1.1. No heat flux

Resulting RTD curves and associated BFs from computational simulations for the no heat flux condition with a 5°C influent for various flow rates are presented in Figures 4.5 and 4.6, respectively.

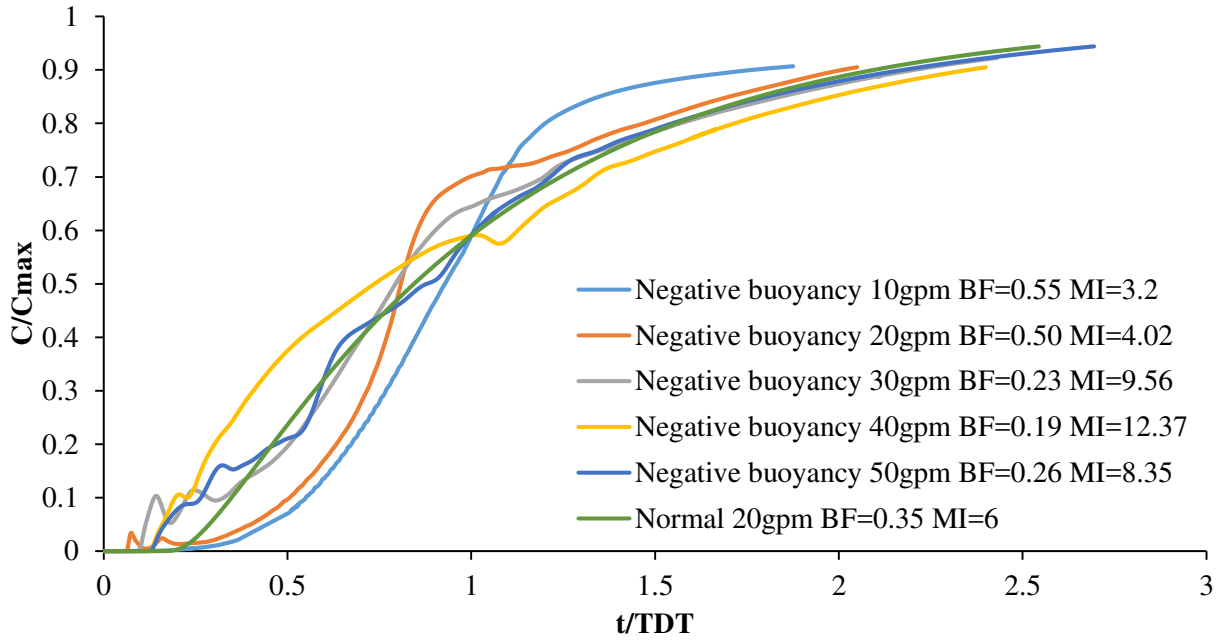


Figure 4. 5 RTD curves under no heat flux condition at various flow rates

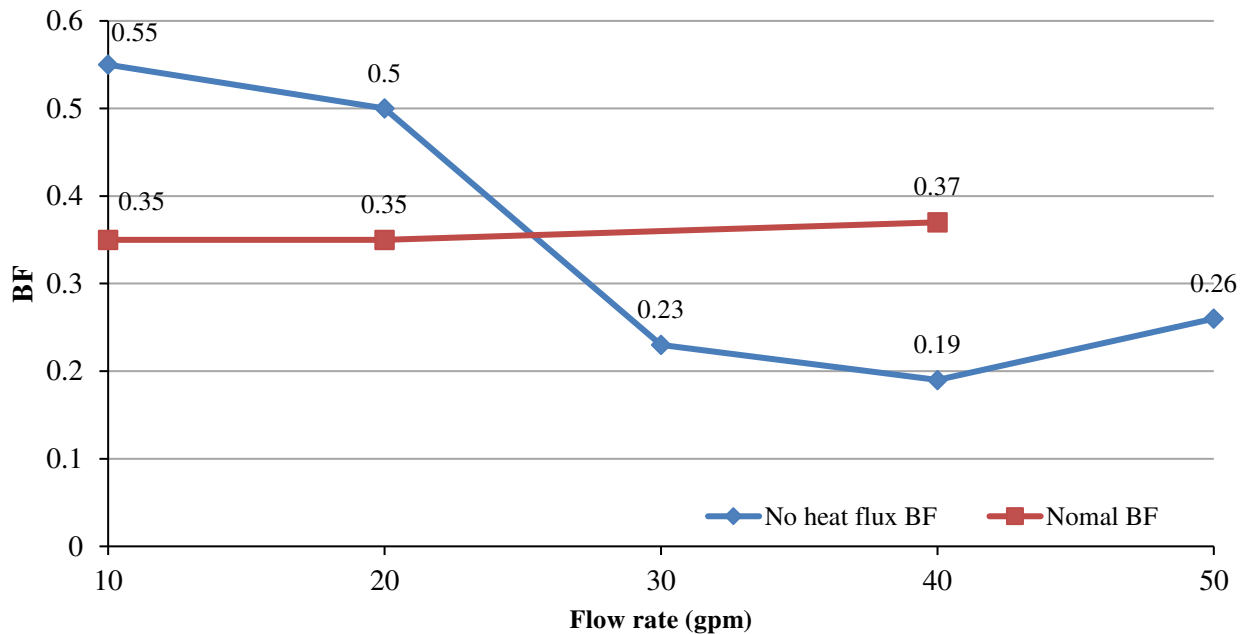


Figure 4. 6 BFs under no heat flux condition at various flow rates

Figure 4.5 shows considerable differences in the RTDs for varying flow rates. In general, the BF decreases with increasing flow rate (as shown in Figure 4.6) but went slightly up at the highest flow rate of 50 gpm. The noticeable fluctuations in the rising limb of the RTD curves in Figure 4.5 can be attributed to the transient changes in the distribution of the temperature in the tank. It can be seen from Figure 4.6 that there was a noticeable drop in BF between 20 and 30 gpm. A plausible reason might be that the flow mostly likely transitions from laminar to turbulent state. At higher flow rates than 30 gpm, the BF appears to be relatively constant. At the lower flow rates (i.e. 10gpm and 20gpm), the BFs are greater than the neutral case, while at higher flow rate (i.e. 30gpm, 40gpm, and 50gpm), BFs are lower. At 10gpm, the stably stratified flow condition results in an increase of 57% in BF compared to the neutral case while at higher flow rate of 40 gpm, the BF decreases by 49% relative to the neutral case. It is the decrease in BF that poses a problem as far as disinfection is concerned.

It is worth noting that the flatter slopes of the rising limbs of the RTD curves for 10 gpm and 20 gpm cases signify the enhanced presence of dead zones at the top of the tank due to strong suppression of the flow in the vertical by buoyancy effects. More details on the flow structure within the tank will be discussed in section 4.4.2.

4.4.1.2. Constant Wall Temperature

A total number of six simulations were performed at various flow rates. The RDT curves and associated BFs under the assumption of constant wall temperature (20°) and with a 5°C influent are presented in Figure 4.7 and Figure 4.8.

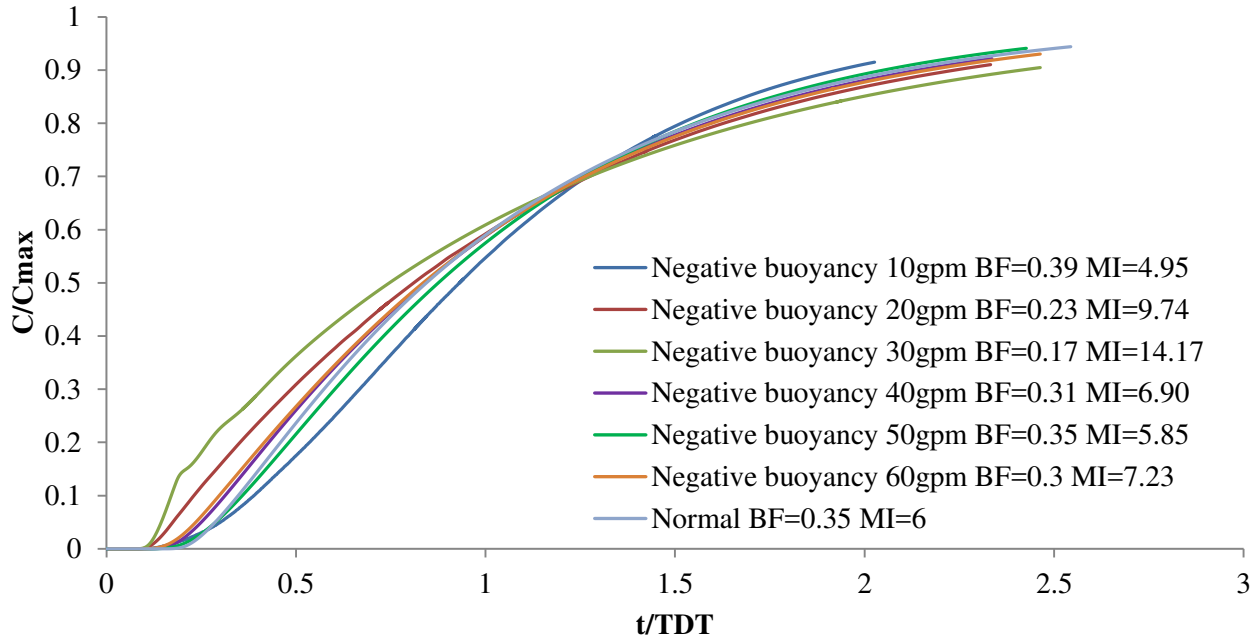


Figure 4. 7 RTD curves under constant wall temperature condition at various flow rates.

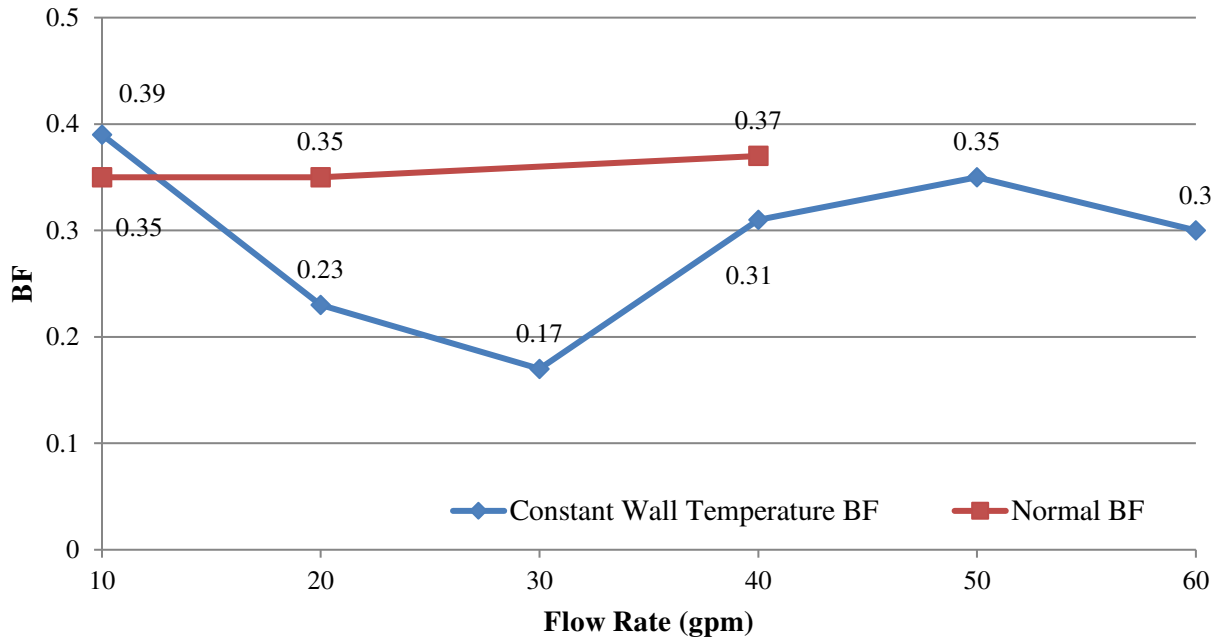


Figure 4. 8 BFs under constant wall temperature condition at various flow rates

Figure 4.8 shows that the BF reaches a minimum value at a flow rate of 30gpm. In this scenario, at a lower flow rate (i.e. 10gpm), the BF increased by 14% while for a transitional flow rate (e.g. at 30gpm), the BF dropped to less than half of the value for the neutral flow case. Interestingly, however, as the flow rate increases further, the BF increases up again and stays close to the BF for the neutral case. Moreover, it can be seen from Figure 4.7 that the RTD curves for constant wall temperature condition were quite smooth throughout the entire process compared to those for scenario 1 (see Figure 4.5). This is simply the flow reaches a steady state condition and hence the temperature does not change during the transient stage of the simulation when the passive scalar is introduced.

In summary, the BF trends for both conditions are similar. With increasing flow rate, the flow would transfer from laminar to turbulent. In the laminar regime, associated BFs were greater than neutral BF, but when the flow became transitional to turbulent, the BF drops below

the BF for the neutral case. Again, it is important to account for the reduction in the BF in order to avoid inadequate inactivation of microbial pathogens in the water.

4.4.1.3. Richardson Number

The Richardson number is a non-dimensional number that can be used to assess the effects of buoyancy on the hydraulic performance of a system. It provides a measure of the effects of buoyancy to shear production (Lin, Hasan & Nyland, 1993). A large (and positive) Richardson number indicates a buoyancy-affected system. It can be defined quantitatively as

$$Ri = \frac{g\beta(T - T_o)L}{v^2} \quad (4.7)$$

In this study, the calculation of Richardson number is based on the initial jet subcooling, jet submergence depth, and jet velocity. As it is expressed in equation 4.8, β is the thermal expansion coefficient that describes how the size of an object changes with change in temperature and its value varies for different fluids at different temperatures. T is the influent temperature and the reference temperature T_o is the surface temperature at t_{10} . L is characteristic length, or the jet submergence depth, and v is the characteristic jet velocity. Typically, when the Richardson number is greater than 0.2-0.25, turbulence can be suppressed by buoyant force, and thus buoyancy effect is considered essential; when $0.1 < Ri < 0.2$, both buoyant and turbulent forces are important and cannot be ignored; and for $Ri < 0.1$, the buoyancy effect can be considered negligible (Grachev, Edgar, Christopher, Guest, & Persson 2012).

Figures 4.9 (A) and (B) show BF with respect to Richardson number for various flow rates with 5°C influent, under no heat flux and constant wall temperature conditions, respectively. The flow rate, indicated by different markers, decreases from left to right in both figures, and the corresponding Richardson number goes up with decreasing flow rate. Hence, the small value of Richardson number can be obtained by increasing the jet velocity. For this

specific disinfection tank, the value of Richardson number ranges from 0.01 to 0.43 under no heat flux condition. As shown in Figure 4.9 (A), the effect of buoyancy on the BF, or hydraulic disinfection efficiency, is negligible for $Ri < 0.05$. Similarly, Figure 4.9 (B) indicates that when the temperature of the tank wall is constant, Richardson number ranges from 0.01 to 0.39. For large Richardson number ($Ri > 0.03$), flow rate could influence the BF remarkably, while the BF is independent with flow rates for low Richardson numbers. With increasing flow rate, turbulence effect dominated the flow regime gradually, so buoyancy influence faded out.

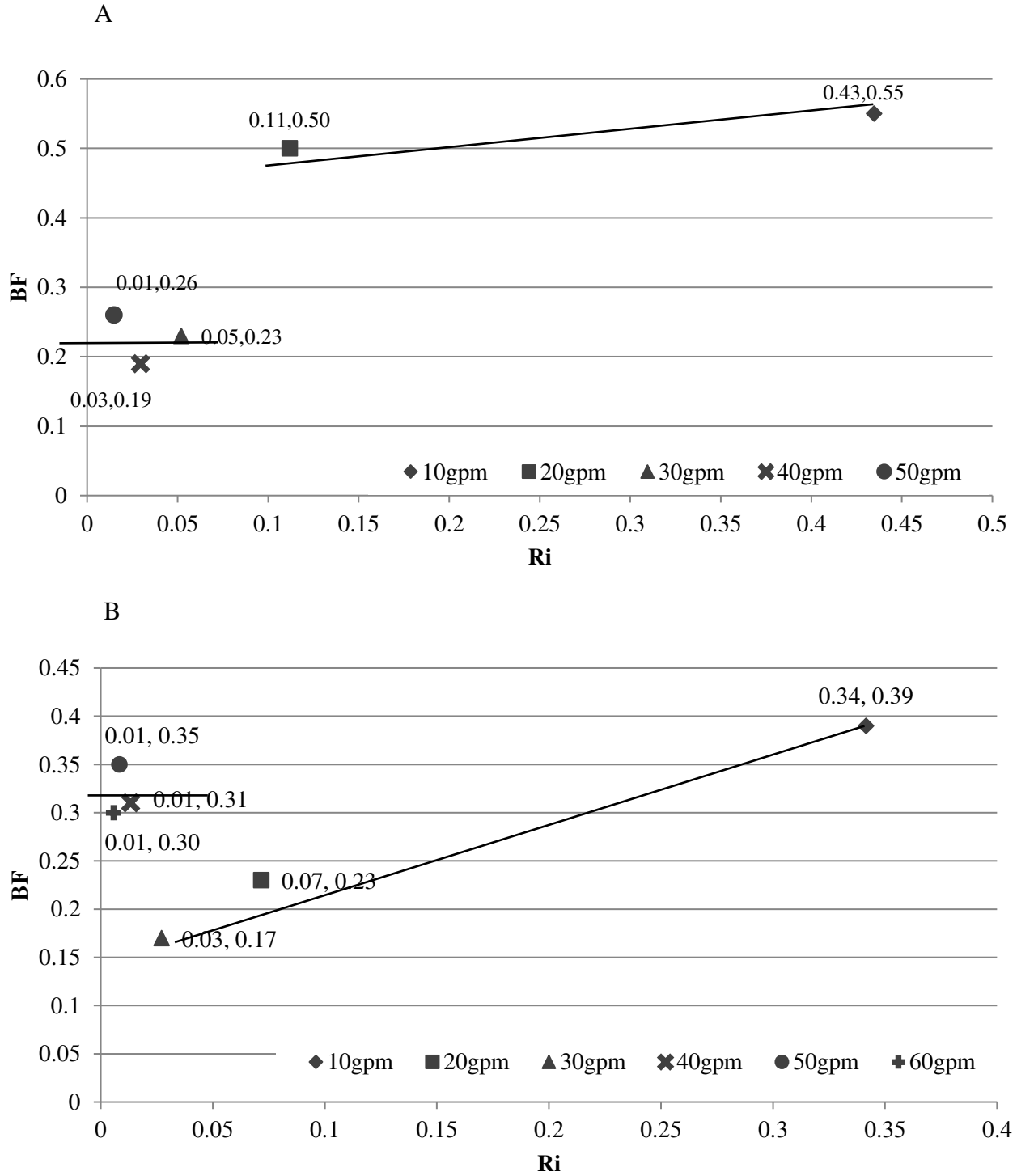


Figure 4. 9 BFs and Richardson numbers under no heat flux condition (A) BFs under constant wall temperature condition (B) at various flow rates

4.4.1.4. Results for 10°C and 15°C influent temperature

It is clear that the buoyancy effect plays an important role at low flow rates. The temperature difference could also be a pivotal factor to determine the hydraulic efficiency of disinfection systems. For simplicity, only the no heat flux condition was considered to explore other values of temperature differences. Figure 4.10 (A) and Figure 4.10 (B) show the RTD curves at 20 gpm and 40 gpm for temperature difference of 10°C and 5°C, respectively. From Figure 4.10 (A), a decrease in flow rate from 40 gpm to 20 gpm could increase BF by 80% for a 10°C temperature difference. On the other hand, Figure 4.10 (B) depicts that BF decreased by 14% when for a 15°C influent, or 5°C temperature difference. It could be clearly seen that the two RTD curves at different flow rates are more similar with small temperature differences (e.g. for as 5°C as shown in Figure 4.10 (B)). When the temperature difference decreases to zero, the RTD curves become nearly identical at various flow rates, as discussed in chapter 3. Therefore, the RTD curves are more sensitive to flow rate for large temperature differences.

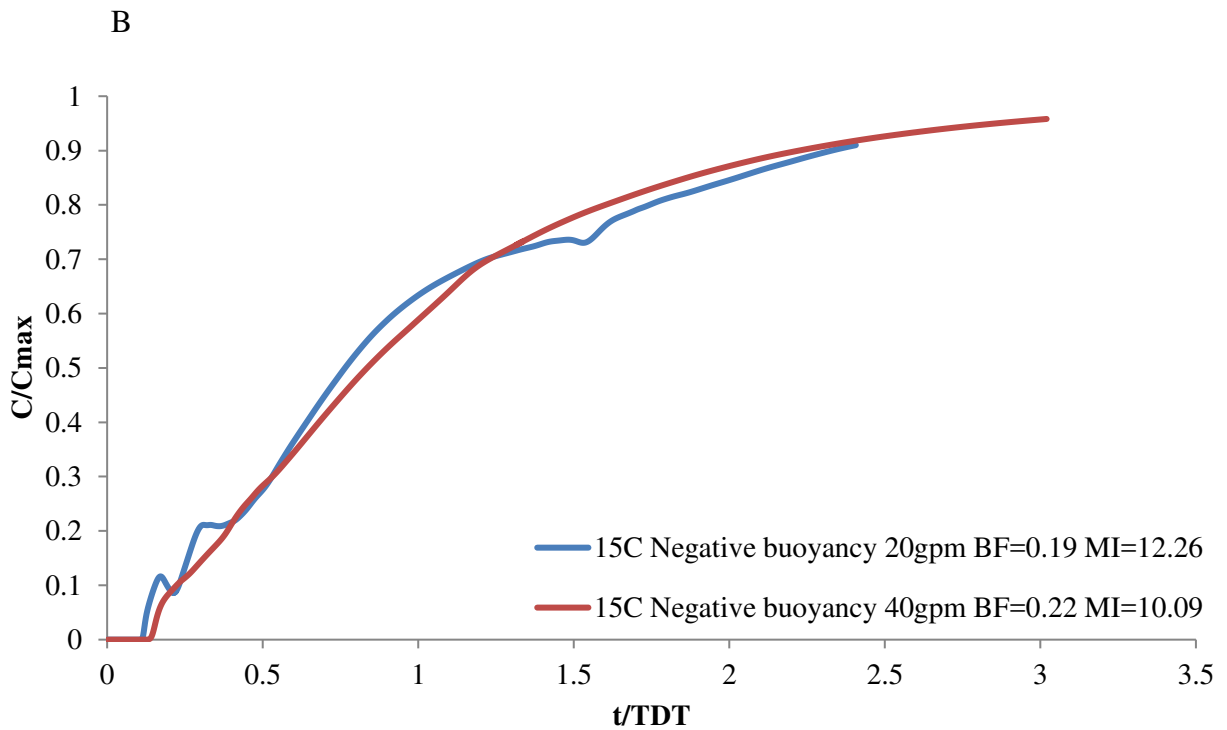
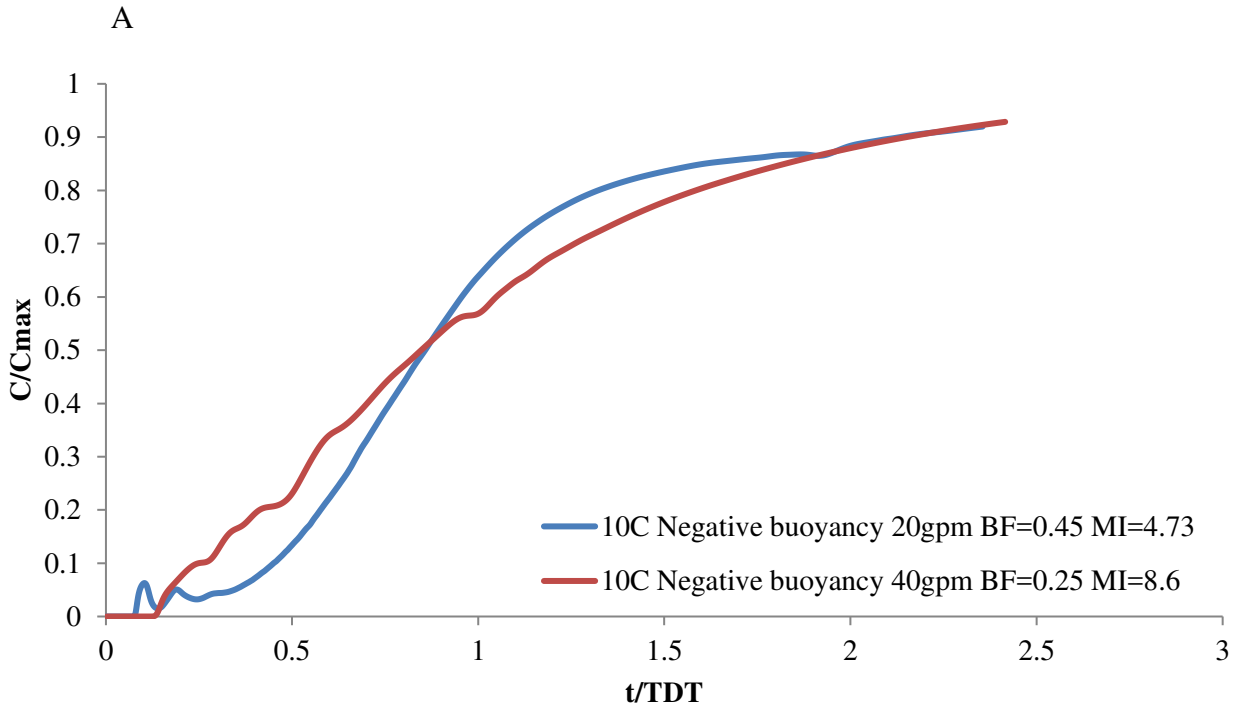


Figure 4. 10 RTD curves with 10°C temperature gradient (A) RTD curves with 5°C temperature gradient (B) at 20gpm and 40gpm

From the RTD curves, the quantitative indicators of hydraulic disinfection efficiency, such as BF and MI, were obtained at two different flow rates with various temperature gradients. Figure 4.11 shows BF with respect to temperature difference at 20 gpm and 40 gpm. Again, the result confirms that at low flow rate (i.e. 20 gpm), the BF is more sensitive to temperature differences. This also restates the fact that buoyancy plays a more important role at a low flow rates. At 20 gpm, the BF continuously went up with increasing temperature difference due to increasing buoyancy effects. The lowest BF occurred at 5°C temperature difference, and the highest BF was at 15°C. The baffling factor increases by 163%. On the other hand, BF dropped initially from the neutral value, and stayed relatively constant at 40 gpm. Based on these trends, it may be conjectured that when the temperature difference is large enough to introduce density currents, the BF will possibly increase and asymptote to a maximum with increasing temperature differences at low flow rates. On the other hand, at high flow rates, the BF may stay relatively constant regardless of the temperature differences, due to the high energy levels in the incoming flow.

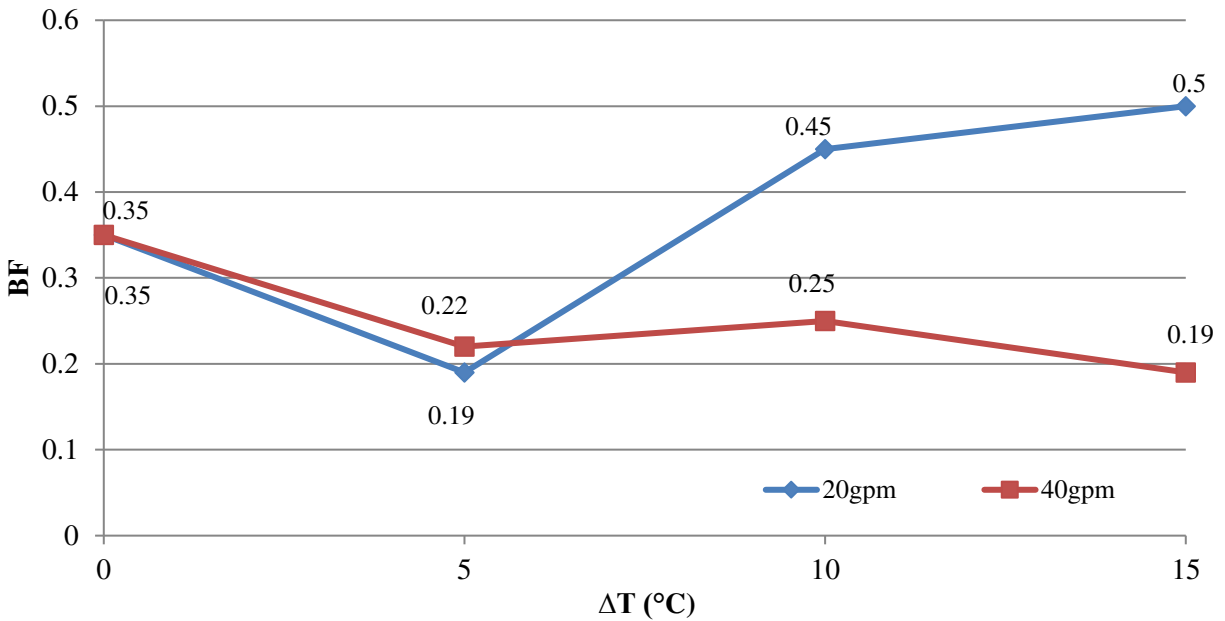


Figure 4. 11 BF with respect to temperature difference at 20gpm and 40gpm

4.4.1.5. Results for top inlet-bottom outlet configuration

It has been discussed in chapter 3 that inlet/outlet location does affect the hydraulic disinfection efficiency of a system. The top inlet-bottom outlet configuration provided the highest hydraulic disinfection efficiency. A key question then is does this high efficiency hold for buoyancy affected flow conditions? The answer is somewhat obvious given that the negatively buoyant inflow will plunge faster and escape quickly through the outlet. To test this rather intuitive assertion, CFD simulations were performed for a top inlet-bottom outlet configuration at 20 gpm and 40 gpm, with 5°C influent. Results are presented in Figure 4.12. The two steep curves are the RTDs for top inlet-bottom outlet tank with negative buoyancy introduced, indicating that the hydraulic disinfection efficiency dropped dramatically for this configuration. With a BF far less than 0.1, the top inlet-bottom outlet baffled tank influenced by negative buoyancy will indeed be a poor design, even though it does give a BF as high as 0.4 for uniform temperature conditions. Indeed, as speculated, the denser and colder influent plunges

from the top to the bottom and flows out of the tank through bottom outlet. Thus, the majority of inflow would find the shortest way to escape the system promoting severe short-circuiting. In contrast, as shown discussed previously, the flow through a tank with a bottom inlet-top outlet configuration experiences the opposite effect.

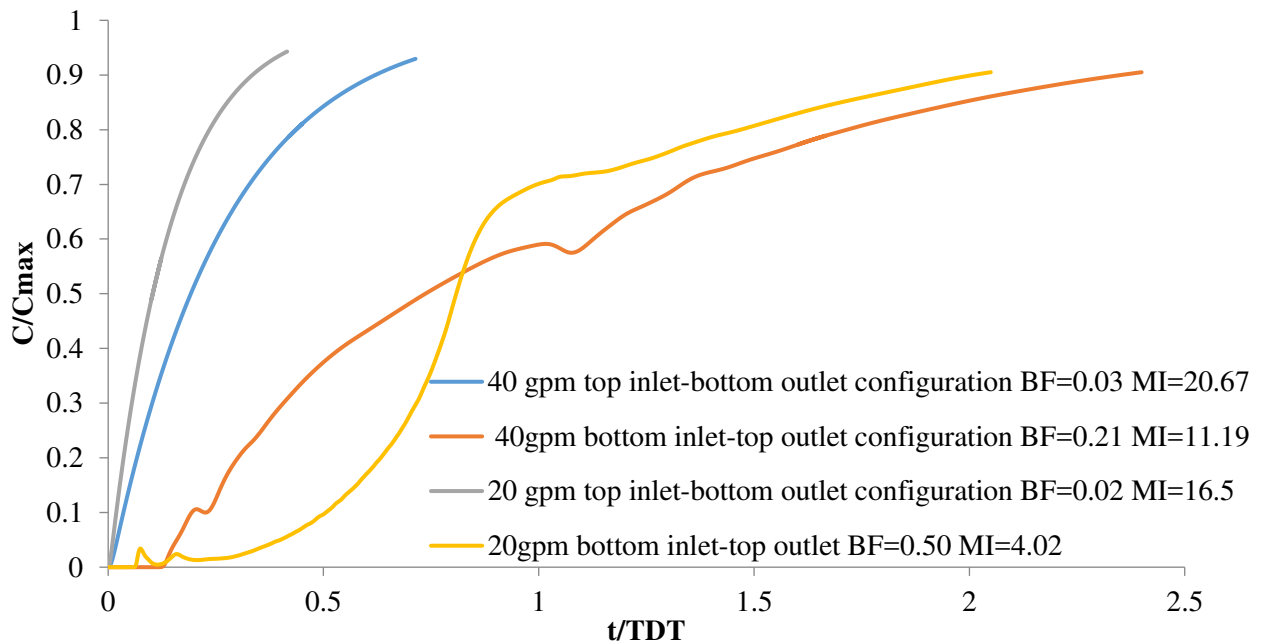


Figure 4. 12 RTD for top inlet-bottom outlet and bottom inlet- top outlet configuration at 20gpm and 40gpm

4.4.2 Flow pattern

In order to investigate the buoyancy effects on hydrodynamics of disinfection systems, instantaneous streamline and associated temperature distribution at 20gpm and 40gpm are illustrated and discussed for both scenarios. For ease of visualization, each streamline was assigned identical color in Figures 4.13 and 4.15. In Figures 4.14 and 4.16, the temperature distributions along three vertical planes that are located in the middle of each baffle channel are displayed.

4.4.2.1 No Heat Flux

Twenty instantaneous streamlines and the associated temperature distribution for a 5°C influent at 20 gpm are shown in Figure 4.13 (A-D), and Figure 4.14 (A-C), respectively.

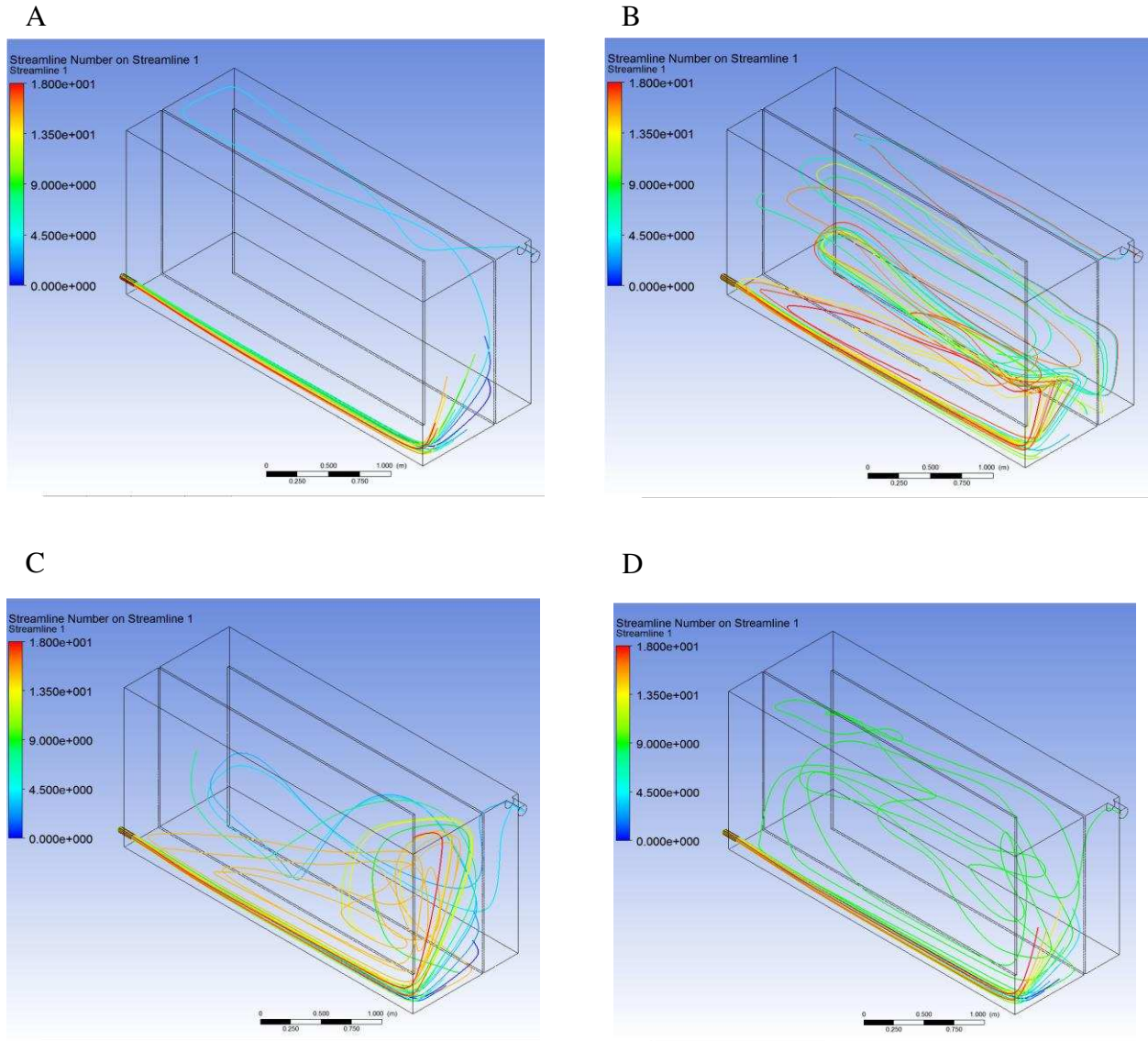


Figure 4. 13 20 gpm instantaneous streamline under no heat flux condition at 0s (A), 900s (B), 3300s (C), and 7800s (D)

Shortly after achieving a steady state flow with uniform temperature, cold and dense water is injected into the system. A big donut-like flow pattern forms around the center of the

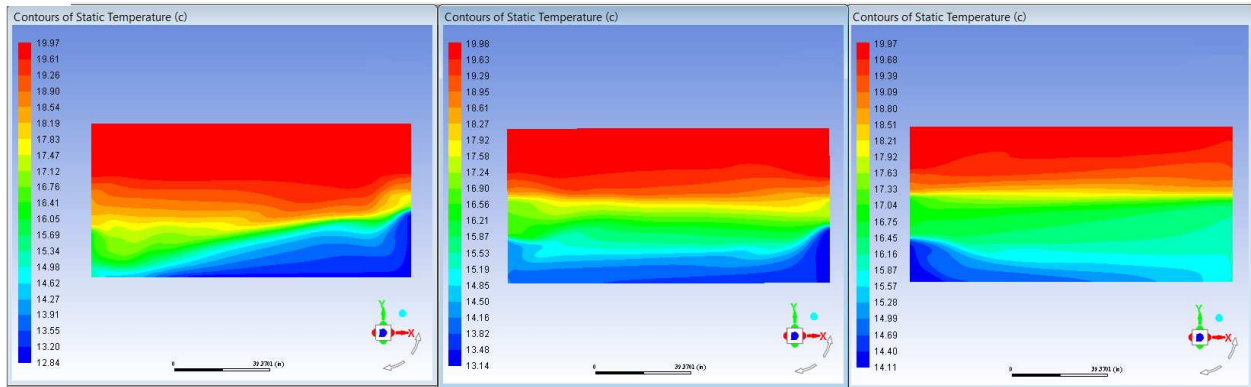
channel (Figure 4.13A) where a large dead zone appeared. Later in time, the water becomes stably stratified, especially at the tank bottom. At 900 s, the momentum was not large enough to raise the new coming water to the water surface, thus a triangular flow regime was formed at the lower back corner of the first channel (as seen in Figure 4.13B). The stratification prevents the inflowing jet to penetrate through the intersection layer. Hence, the majority of the new coming water tends to reside longer at bottom in the second channel and enters the third channel from lower depths. To some extent, this “layer by layer lift” motion expanded the length of baffled channel, and thus increases the BF. This flow structure was maintained for a relatively long period within the procedure. At 3300 s, two main circulations patterns appear in the second channel. The dominant circulation was near the back wall and the other was at the upper left.

Cold water would fill the tank gradually, so the system became less and less stratified. As a result, the back wall circulations enlarged and forced the other circulation out. Finally, the flow pattern would return to original.

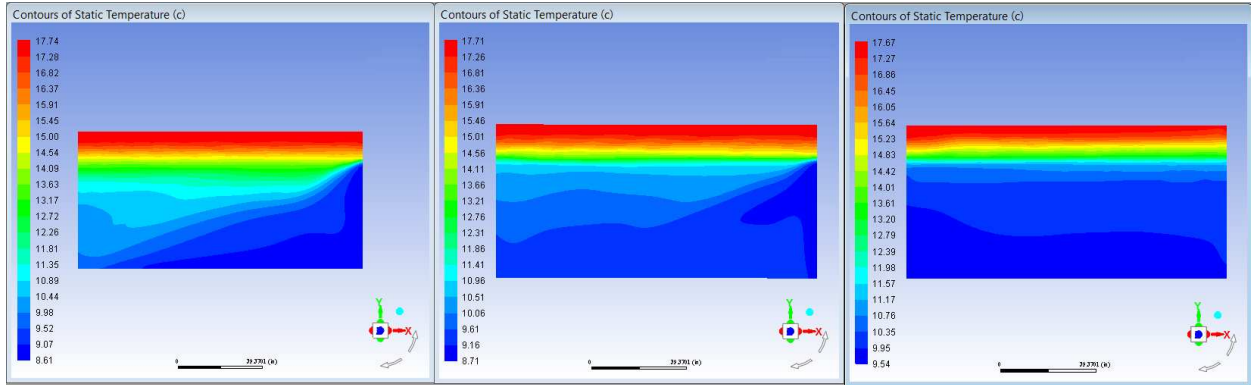
As a comparison, Figure 4.15 (A-D) shows the streamlines at 40 gpm. The streamlines for the 40gpm flow is more chaotic than they were at 20 gpm. As illustrated in Figure 4.15 (B), within the energetic flow, two main circulations patterns appear in the second channel at early stage. The dominant circulation is a counter clockwise circulation near the back wall, resulting from the wall effect. The other circulation is also counter clockwise at the upper left (too small to be visible in figure). These circulations generate many small dead zones and thus contribute to low hydraulic disinfection efficiency. This flow structure was preserved for the majority of the procedure, until the cold inlet jet reached the water surface. Eventually, similar to the flow at 20gpm, the flow structure returned to the beginning as the cold water filled the tank.

Figure 4.14 (A-C) presents the temperature distributions for a 5°C influent at 20gpm. It provides another perspective for understanding the changes in flow pattern. From left to right, it displays the temperature along vertical planes in the middle of the first, second, and third baffle channels, respectively. Red color indicates high temperature, and blue indicates low temperature. The temperature distribution of the system drops from bottom to top along the streamline. Figure 4.14 (A) is the most long lasting temperature distribution at 20 gpm. The flow was well stably stratified, which suppressed the vertical mixing. Hence, vertical homogeneity could be easily obtained within layer. As shown in Figure 4.14 (B) and Figure 4.14 (C), an unstable stratification occurred at 3300 s and became more visible at 4350 s. This is because a counter clockwise circulation appears near the back wall, which may contribute to a decrease in hydraulic disinfection efficiency in later process.

A



B



C

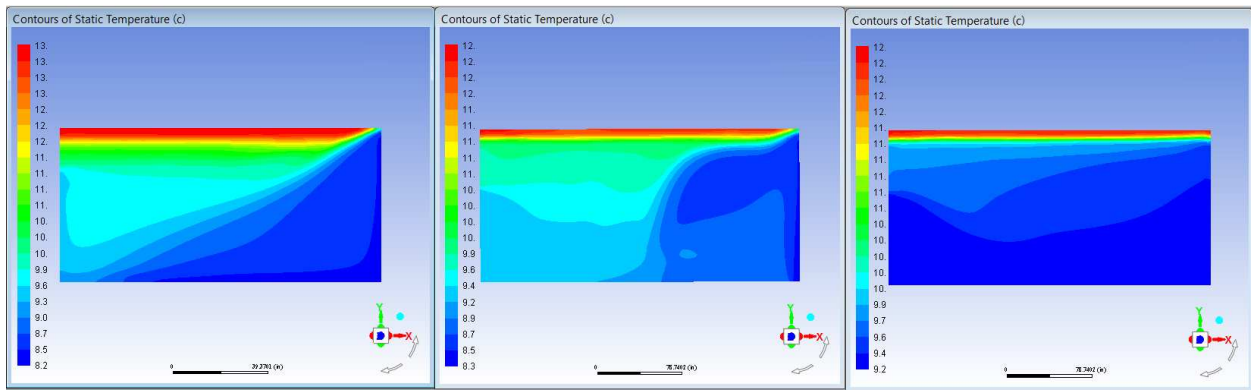


Figure 4.14 20 gpm temperature distributions for a 5°C influent under no heat flux condition at 900s (A), 3300s (B), and 4350s (C)

Figure 4.16 (A-C) show the temperature distributions at 40 gpm. Similar to 20gpm, at 40gpm, stratification begins to form during the earlier stages of the transient process. Because of larger momentum, the jet was able to reach the water surface when it hit the back wall. A reversed L-shape regime with lower temperature was formed near the back wall around the first baffle turn opening. Unstably stratified flow persisted during entire process, and promote turbulence in vertical direction. However, this large scale vertical mixing made it hard to achieve homogeneous vertical velocity.

In summary, the flow at 40gpm is more chaotic and turbulent, and thus more dead zones and short-circuiting appeared in the system. Therefore, as alluded to in previous discussion, the BF for high flow rate is lower than the BF for low flow rate.

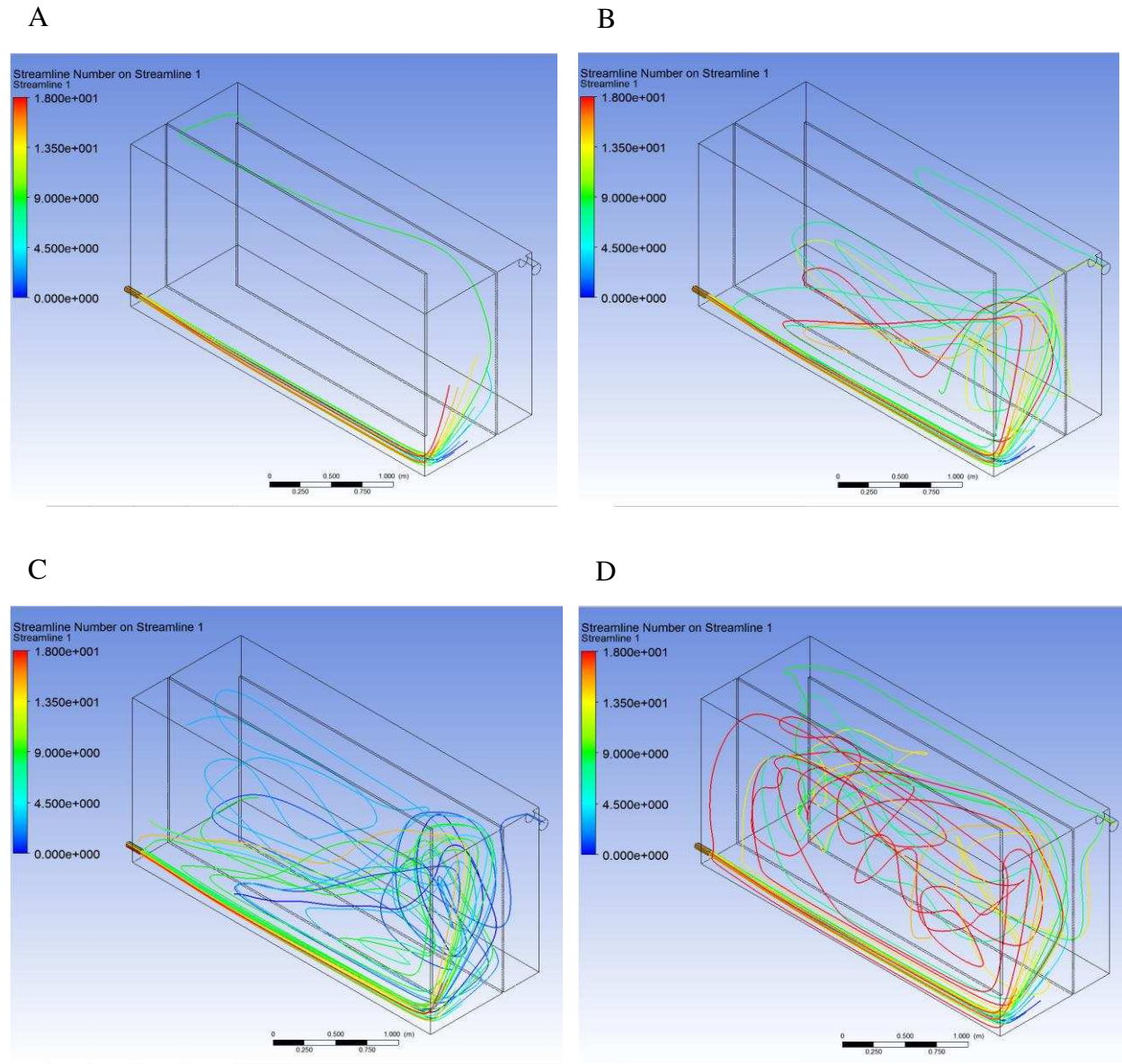
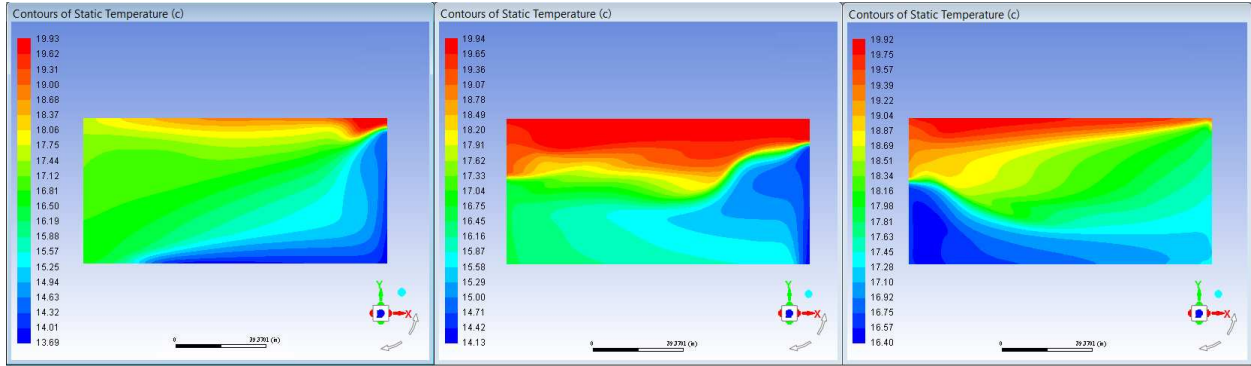
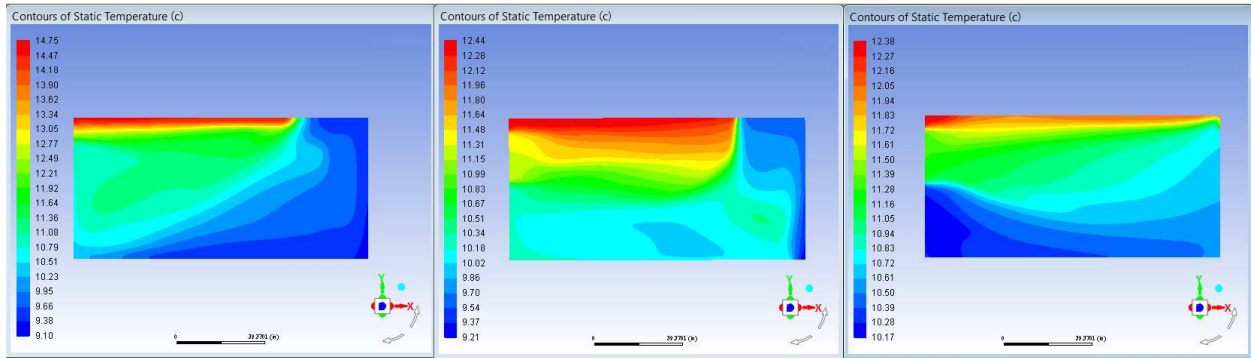


Figure 4. 15 40 gpm instantaneous streamline under no heat flux condition at 0s (A), 525s (B), 2450s (C), and 2800s (D)

A



B



C

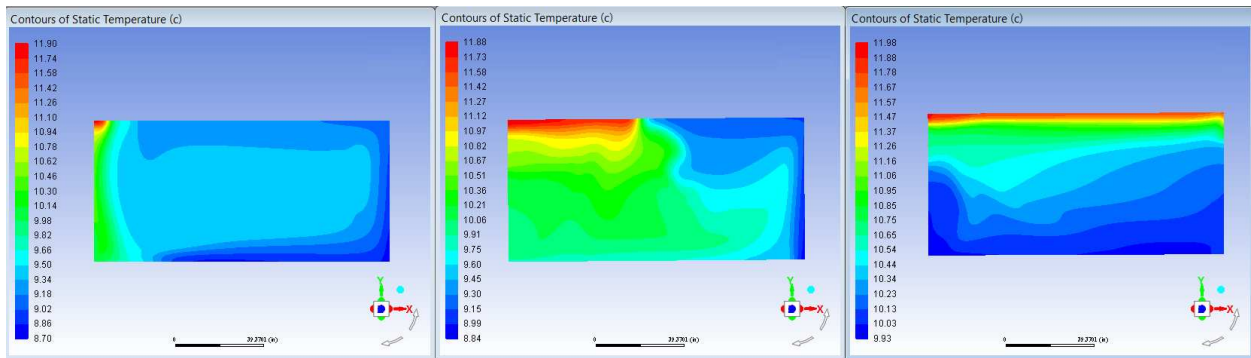
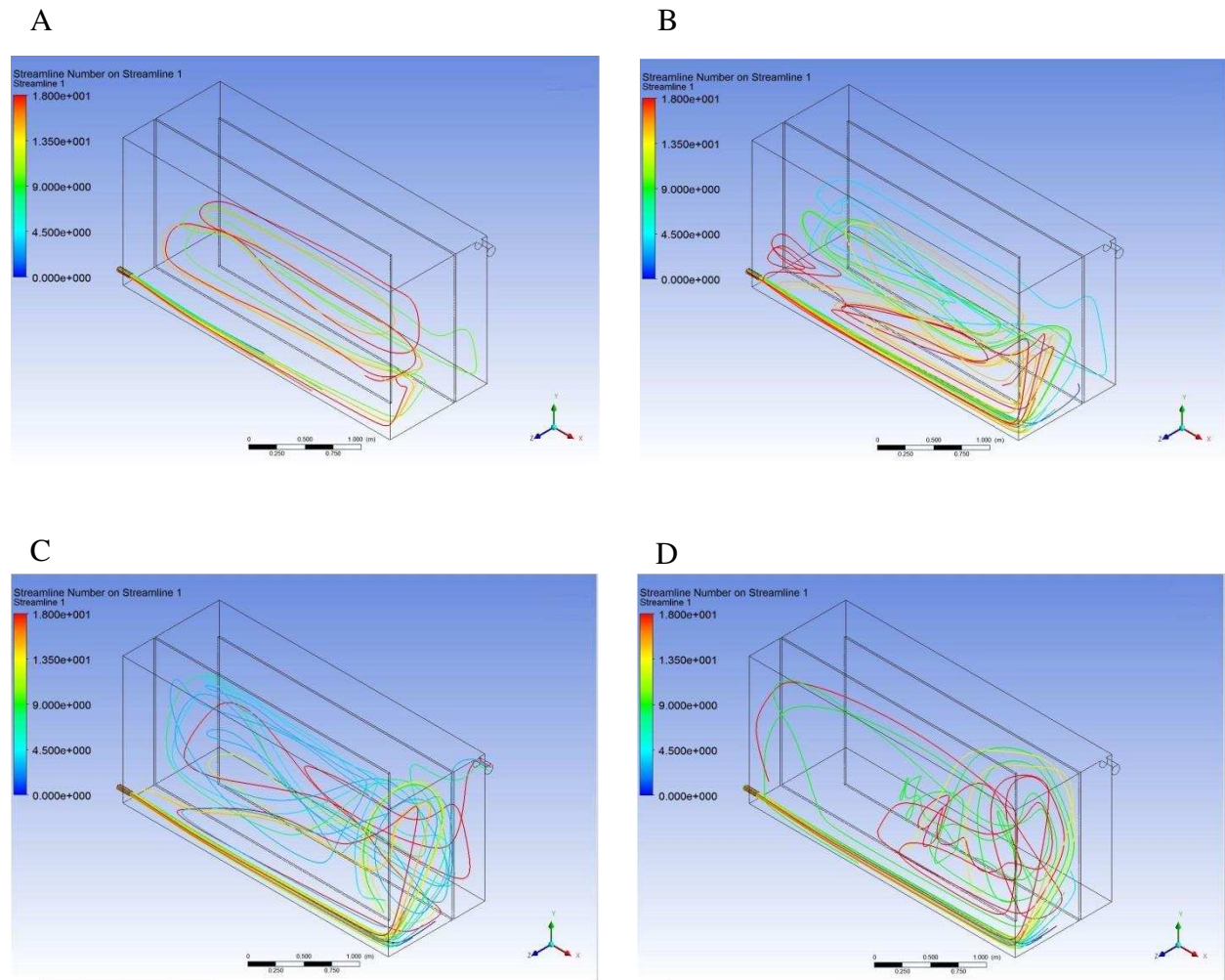


Figure 4. 16 40 gpm temperature distributions for 5°C influent under no heat flux condition at 525s (A), 2450s (B), and 2800s (C)

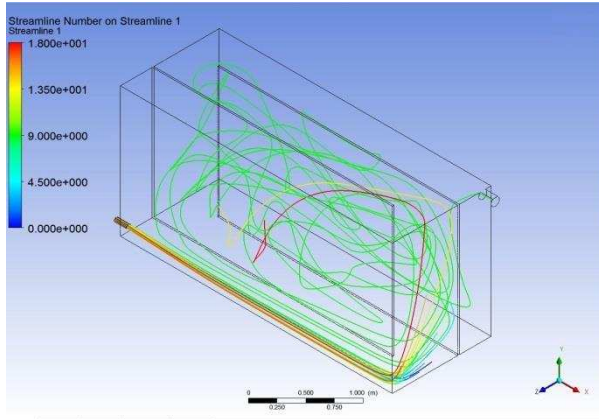
4.4.2.2 Constant Wall Temperature

Under the assumption of constant wall temperature (20°C), steady state was achieved before tracer was introduced; hence, temperature distributions and velocity fields remained

unchanged. Figure 4.17 and Figure 4.18 show the steady streamlines and temperature distributions at various flow rates. Twenty streamlines were generated from inlet and the color represented for streamline identity. Figure 4.17 (A-F) presents the streamline at 10 gpm, 20 gpm, 30 gpm, 40 gpm, 50 gpm, and 60 gpm, respectively. The flow became more turbulent with increasing flow rates. The associated temperature distributions are showed in Figure 4.18 (A-F).



E



F

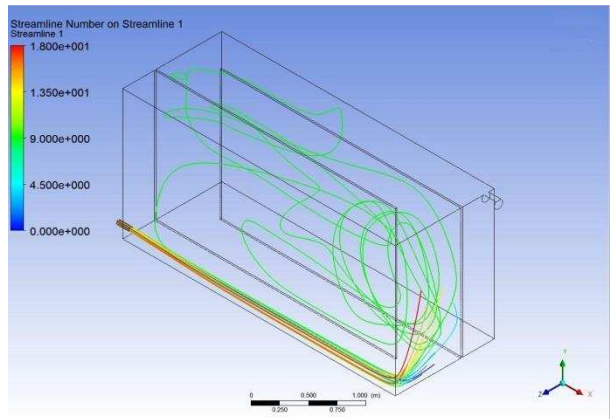
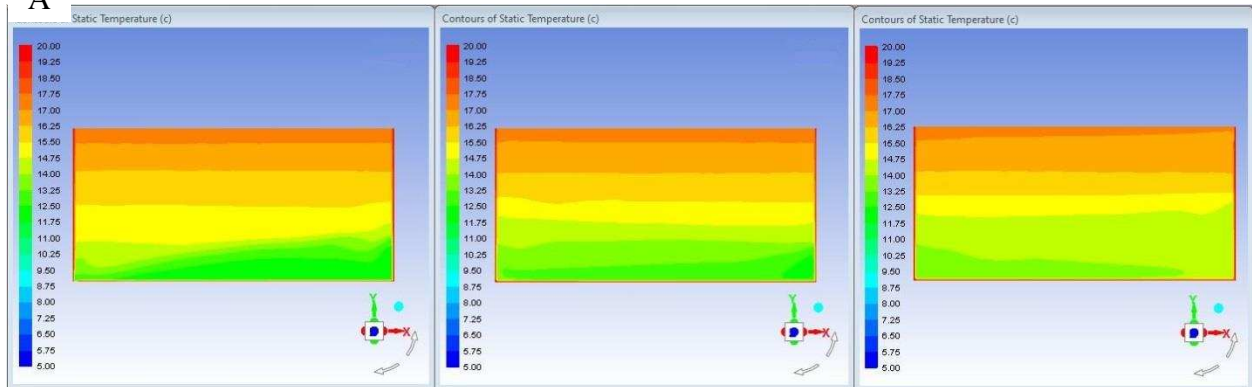
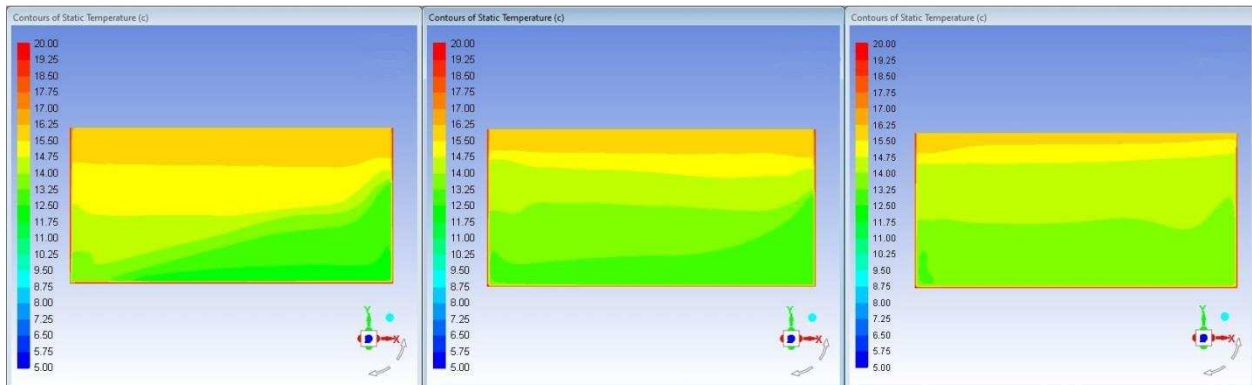


Figure 4. 17 Steady streamline under constant wall temperature condition at 10gpm (A), 20gpm (B), 30gpm (C), 40gpm (D), 50gpm (E), and 60gpm (F)

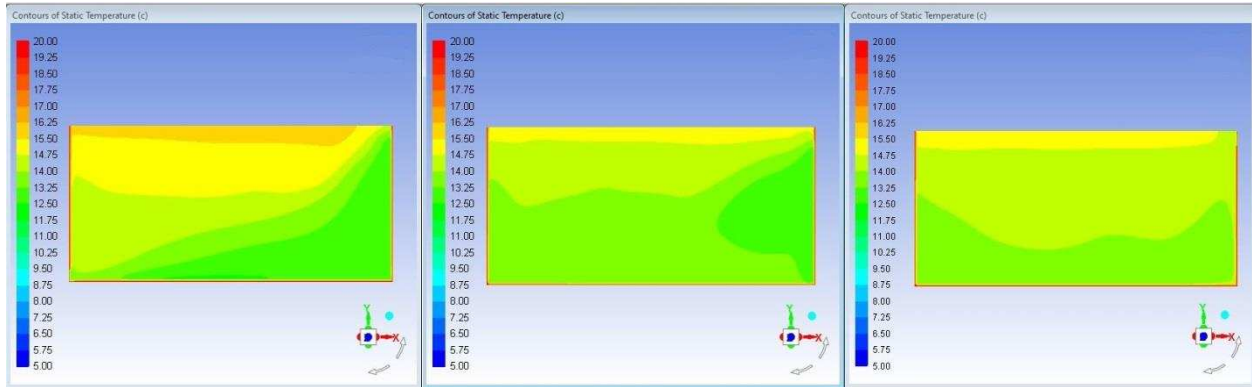
A



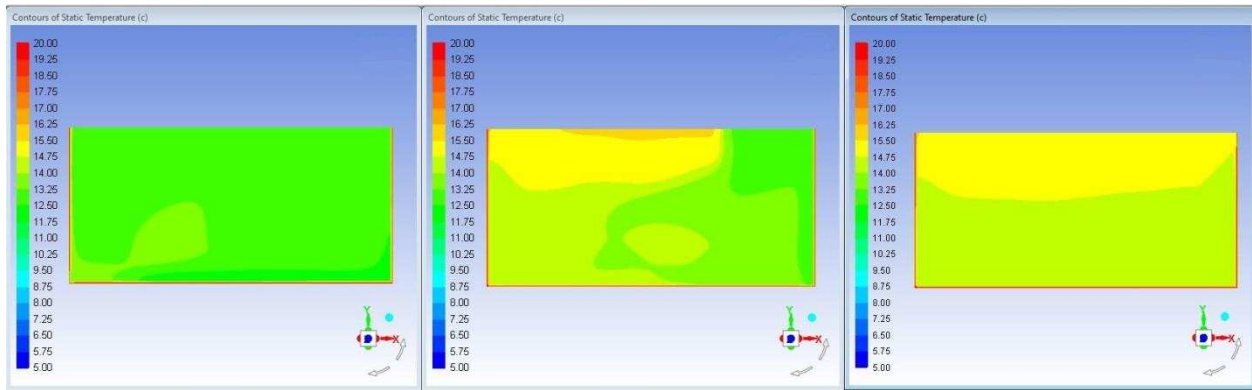
B



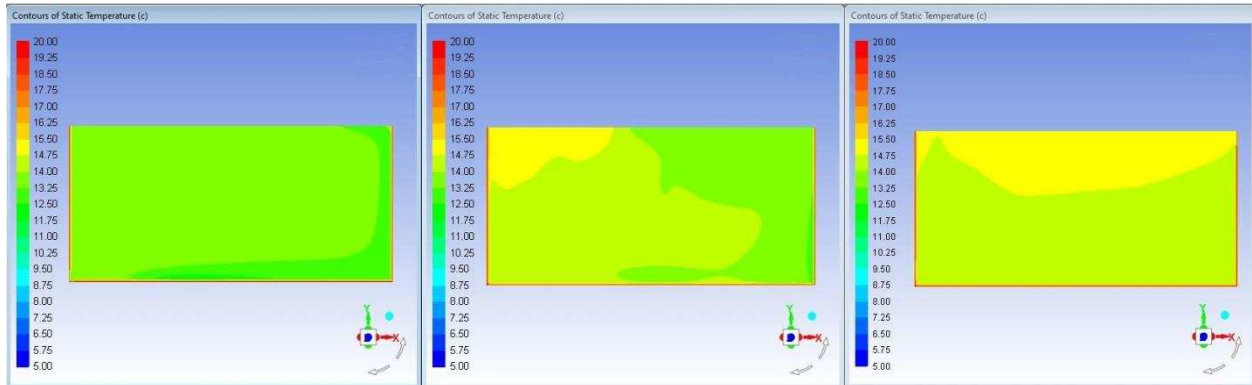
C



D



E



F

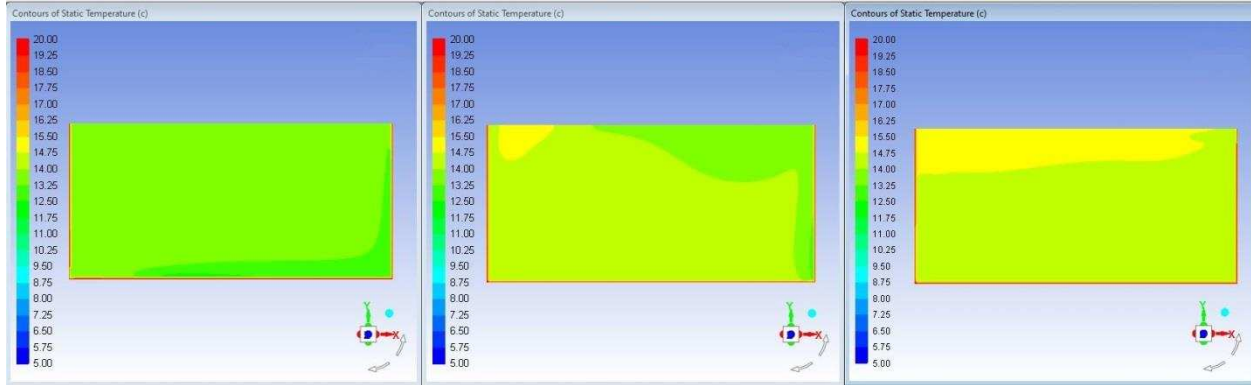


Figure 4. 18 Steady temperature distribution under constant wall temperature condition at 10gpm (A), 20gpm (B), 30gpm (C), 40gpm (D), 50gpm (E), and 60gpm (F)

As shown in Figure 4.18, the stratification diminishes with increasing flow rate. It is also clear from Figure 4.17 and Figure 4.18 that at lower flow rates (< 40 gpm), the momentum of new coming flow was not large enough to penetrate vertically. More temperature layers are evident at 10gpm, and the temperature distribution did not change significantly among the three channels. This flow structure contributed to a “layer by layer lift” motion and made a longer path for the flow. Lesser extent stratifications are seen in Figure 4.18 (B) and Figure 4.18 (C). These stratifications, on the contrary, promoted vertical mixing in a relatively large scale, so vertical homogeneity was hard to obtain, resulting in a decrease in hydraulic disinfection efficiency. When the flow rate was greater than 40gpm, the incoming flow was able to reach the water surface. The energetic influent had sufficient momentum to mix vertically and thus, BF went up.

4.5 Conclusion

This study highlights the importance of buoyancy effects in disinfection systems. A rectangular baffled disinfection contact tank was used to investigate the problem. Hydraulic disinfection efficiency was estimated using RTD curves and baffling factor. The flow pattern was probed by visualizing flow patterns using streamlines and temperature distributions.

For the no heat flux condition, the disinfection system performed better than neutral case at low flow rates, but the hydraulic disinfection efficiency dropped below that of the neutral case at high flow rates. Similar trends were obtained for the constant wall temperature condition, but the difference between the highest and lowest BF compared to the neutral case BF were not as large as those for the no heat flux case.

In summary, this preliminary study underscore the complexity associated with buoyancy effects that can occur in disinfection contact tank due to temperature differences. It is therefore important to consider fluctuations in temperature due to seasonal variations in assigning disinfection efficiencies of contact tanks.

CHAPTER 5 SUMMARY AND CONCLUSIONS

5.1 Summary of Research

The research conducted and presented in this thesis assesses the effects of different inlet/outlet locations as well as that of buoyancy on the performance of hydraulic disinfection in small drinking water systems. CFD was validated and applied in this study to investigate the hydraulic disinfection efficiency and internal flows in a rectangular disinfection tank. A total of 15 CFD simulations were performed for three inlet/outlet location combinations (i.e. bottom inlet-bottom outlet, bottom inlet-top outlet, and top inlet-bottom outlet) and two outlet sizes (2-in.-diameter and 4-in.-diameter) in both baffled and un-baffled tanks at various flow rates. The residence time distribution (RTD) curves from the simulations were used to obtain the baffling factors.

In Chapter 4, the effect of negative buoyancy on hydraulic disinfection efficiency of a contact tank was investigated by introducing a colder influent into the tank. The temperature of influent could vary seasonally and generate density currents in the system once introduced into an ambient fluid of different density. This practical problem is ignored in previous studies on this topic, and may result in overestimation of disinfection performance of contact tanks. Two conditions were simulated to understand the buoyancy effect in disinfection tanks. The first is a no heat flux condition between walls and the fluid. The second scenario is a heated wall condition where the temperature is held at constant value on all walls (including baffles) while inflowing water is at a lower temperature. CFD simulations of flow and scalar transport in a concrete rectangular tank with various temperature differences and flow rates were then

performed for both conditions. Resulting RTD curves and associated BF were obtained and the results were discussed using hydrodynamic analysis of the CFD simulations.

5.2 Major Conclusions

In Chapter 3, the baffling factors for the un-baffled tank were too low (< 0.1) to give satisfactory disinfection performance as per the United States Environmental Protection Agency (USEPA) standards, regardless of the locations of the inlet/outlet. On the other hand, the effect of the locations was significant for the baffled tank. For the latter case, the baffling factor ranged from 0.3 (for the bottom inlet-bottom outlet configuration) to 0.4 (for the top inlet-bottom outlet configuration), indicating that different configurations of the inlet/outlet location can result in gains in baffling factor in excess of 30%. The results also indicated that given the same tank geometry, the flow rate and small alteration of outlet size do not affect the hydraulic disinfection efficiency.

Research presented in Chapter 4 showed that the buoyancy effect can be significant in disinfection systems, especially for a system at low flow rate and with large temperature gradient. Negative buoyancy could increase hydraulic efficiency at low flow rates, but reduce the hydraulic disinfection efficiency at high flow rates. For the no heat flux condition, negative buoyancy with a 15°C temperature difference would improve the hydraulic performance of a system by 57% at 10gpm. However, at 40gpm, it decreased the BF by 49%. For a constant 20°C wall temperature condition, at a flow rate of 10gpm, the BF increased by 14%, but at 30gpm, the BF dropped to less than half of the BF obtained for the neutral flow case with no temperature differences. A dramatic drop occurred in BF between low flow rate and high flow rate under both conditions due to the buoyancy effect. Even though with negative buoyancy effect, a low

flow rate could result in gains in baffling factor, the overestimated BF at high flow rate may result in inadequate microbial inactivation that can cause illness.

In summary, this research shows that the effects of inlet/outlet locations and the effect of buoyancy on the hydraulic disinfection efficiency of contact tank can be significant and thus should be given due consideration.

5.3 Recommendation for Further Work

The following recommendations are made for the continuing research on drinking water disinfection systems.

- The contact tanks in this study were modeled as steady state systems, which imply the inflow rate is always equal to the outflow rate. In many real world operating conditions, outlet flow rates can be variable and free-surface elevations are not fixed in time. In order to capture the real-time disinfection efficiency with varied outlet flow rates and variable free-surface elevations, the present study should be extended to include unsteady effects.
- The CFD model presented in Chapter 4 was only validated with uniform temperature. Physical tracer tests with various temperature gradients between influent and storage water need to be conducted to further verify the model.

REFERENCE

- ANSYS Inc. 2009. ANSYS FLUENT Users' Guide. Canonsburg, PA.
- ANSYS Inc. 2013. ANSYS FLUENT Meshing Users' Guide. Canonsburg, PA.
- ANSYS Inc. 2013. ANSYS FLUENT Theory Guide. Canonsburg, PA.
- ANSYS Inc. 2009. ANSYS Workbench Platform. Canonsburg, PA.
- Armenio, V., and Sarkar. S., 2005. *Environmental Stratified Flow*. Springer-Verlag Wien
- Baik, J.J., Kim, J.J., Fernando, H.J.S., 2003. *A CFD model for simulating urban flow and dispersion*, Journal of Applied Meteorology 42, 1636 - 1648.
- Barnett, T.C.; Kattinig, J.J.; Venayagamoorthy, S.K.; & Whittaker, G., 2014. Improving Drinking
- Brzoska, M.A., Stock, D., Lamb, B., 1997. *Determination of plume capture by the building wake*, Journal of Wind Engineering and Industrial Aerodynamics 67&68, 909 - 922.
- Carlston, J.S. 2015. Impact of Geometric Design Of Hydraulic Contact Tanks on Residence Time Distributions. Master's thesis, Department of Civil and Environmental Engineering, Colorado State University, Fort Collins, Colorado, USA.
- Carlston, J.S. & Venayagamoorthy, S.K., 2015. Impact of Modified Inlets on Residence Times in Baffled Tanks. *Journal AWWA*, 107:6:E292.
- Cenedese, Claudia., 2012, *Density current*. Encyclopaedia Britannica.
<<https://www.britannica.com/science/density-current#toc302516>> Accessed 10 February 2017.
- CFD Online. *Codes*. Tecplot, Inc.et al., 7 Feb. 2017.
<<https://www.cfdonline.com/About/sponsors.php>> Accessed 10 February 2017.
- Delaunay, D., 1996. *Numerical simulation of atmospheric dispersion in an urban site: Comparison with field data*. Journal of Wind Engineering and Industrial Aerodynamics 64, 221 - 231.
- DeVantier B. A., and Larock B. E., 1987, *Modeling sediment-induced density currents in sedimentation basins*. Journal of Hydraulic Engineering 113-1, 80-94.
- Flesch, T.K., John, H. P & Jerry, L. H, 2002. *Turbulent Schmidt number from a tracer experiment*. Agricultural and Forest Meteorology 111, 299 - 307.
- Goula, A.M., Kostoglou, M, Karapantsios, T.D., and Zouboulis, A.I., 2008, *The effect of influent temperature variations in a sedimentation tank for potable water treatment-A computational fluid dynamics study*. Water Research 42 (2008) 3405-3414.

- Gualtieri, C. 2006. Numerical simulations of flow and tracer transport in a disinfection contact tank. *International Congress on Environmental Modelling and Software*.
- Guetter A. K., and Jain S. C., 1991. *Analytical solution for density currents in settling basins*. Journal of Hydraulic Engineering 117-3, 324-345.
- Kattnig, J.J. 2014. Use of Innovative Techniques to Optimize the Residence Time Distribution of Drinking Water Contact Tanks. Master's thesis, Department of Civil & Environmental Engineering, Colorado State University, Fort Collins.
- Kattnig, J.J. & Venayagamoorthy, S.K., 2015 A Hybrid Approach for Increasing Baffling Factors in Contact Tanks. *Journal AWWA*, 107:12:E702.
- Kim, D., Stoesser, T., & Kim, J. 2013. The effect of baffle spacing on hydrodynamics and solute transport in serpentine contact tanks. *Journal of Hydraulic Research*, 5:51:558.
- Kim, J-J., Baik, J-J., 2003. *Effects of inflow turbulence intensity on flow and pollutant dispersion in an urban street canyon*. Journal of Wind Engineering and Industrial Aerodynamics 91, 309 - 329.
- Letterman, R.D; ed. 1999. *Water Quality and Treatment, 5th ed*. American Water Works Association, McGraw-Hill: New-York.
- Li, Y. & Stathopoulos, T., 1997. *Numerical evaluation of windinduced dispersion of pollutants around a building*. Journal of Wind Engineering and Industrial Aerodynamics 67&68, 757 - 766.
- Lien, F.S., Yee, E., Ji, H., Keats, A., Hsieh, K.J., 2006. *Progress and challenges in the development of physically based numerical models for prediction of flow and contaminant dispersion in the urban environment*. International Journal of Computational Fluid Dynamics 20 (5), 323 - 337.
- Lin, C.S., Hasan, M.M., and Nyland, T.W., 1993, *Mixing and transient interface and condensation of a liquid hydrogen tank*. NASA Technical Memorandum AIAA-93-1968
- Moin, P. 2010. *Fundamentals of Engineering Numerical Analysis*. Cambridge University Press: New York, NY.
- Munson, Bruce R., Young, Donald F., Okiishi, Theodore H., Huebsch, Wade W., 2009, *Fundamental of Fluid Mechanics, Sixth Edition*. John Wiley & Sons, Inc. Press: the United State of America.
- Pope, S.B., 2000. *Turbulent Flows*. Cambridge University Press: Cambridge, U.K.
- Rauen, W. B.; Angeloudis, A.; & Falconer, R. A. 2012. Appraisal of chlorine contact tank modelling practices. *Water Research*, 46:18:1583.
- Rodrigo, A.B.; Ebeling, M.J.; Bhaskaran, R. & Timmons, B.M., 2007. Effects of Inlet and Outlet Flow Characteristics on Mixed-cell Raceway (MCR) Hydrodynamics. *Aquacultural Engineering*, 37:2:158.

- Santiago, J., Martilli, A., Martin, F., 2007. *CFD simulation of airflow over a regular array of cubes. Part I: Threedimensional simulation of the flow and validation with wind-tunnel measurements*. *Boundary-Layer Meteorology* 122 (3), 609 – 634.
- Stamou, A. I. 2008. Improving the hydraulic efficiency of water process tanks using CFD models. *Chemical Engineering and Processing: Process Intensification*, 47:8:1179.
- Taylor, Z.H.; Carlston, J.C.; & Venayagamoorthy, S.K., 2015. Hydraulic Design of Baffles in Disinfection Contact Tanks. *Journal of Hydraulic Research*, 53:3:400.
- Teixeira, E. C.; Siqueira, R. N. 2008. Performance Assessment of Hydraulic Efficiency Indexes. *Journal of Environmental Engineering*, 134(10), 851-859.
- Tian, X., and Roberts, P. J. W., 2008. *Mixing in water storage tanks. I: No buoyancy effects*. *Journal of environmental engineering*. 134-12, 986–995.
- United States Environmental Protection Agency, USEPA. 2006. *Small Drinking Water System Variances* < <https://www.epa.gov/dwregdev/small-drinking-water-system-variances>> December 1st 2016
- United States Environmental Protection Agency, USEPA. 2012. Safe Drinking Water Act (SDWA). < <http://water.epa.gov/lawsregs/rulesregs/sdwa/>> December 1st 2016
- United States Environmental Protection Agency, USEPA. 2016. (August) *Science in action*. Tech, report EPA 600/F-16/187. USEPA
- United States Environmental Protection Agency, USEPA. 2003. *LT1ESWTR Disinfection Profiling and Benchmarking Technical Guidance Manual*. EPA 816-R-03-004, Office of Water, Washington, D.C.
- USEPA (US Environmental Protection Agency), 2003. *Disinfection Profiling and Benchmarking Guidance Manual*. EPA 815-R-99-013. USEPA Office of Water, Washington.
- USEPA (US Environmental Protection Agency), 2011. *National Characteristics of Drinking Water Systems Serving Populations Under 10,000*. EPA 816-R-10- 022. USEPA Office of Water, Washington.
- USEPA (US Environmental Protection Agency), 2014. *Small Public Water Systems and Capacity Development*. USEPA Office of Water, Washington.
- Venayagamoorthy, S.K. & Stretch, D.D., 2010. On the Turbulent Prandtl Number in Homogeneous Stably Stratified Turbulence. *Journal of Fluid Mechanics*, 644:359.
- Wang, H.; Shoa, X.; Falconer, R.A., 2003. Flow and Transport Simulation Models for Prediction of Chlorine Contact Tank Flow-Through Curves. *Water Environment Research*, 75:5:455.
- Wang, X., McNamara, K.F., 2006. *Evaluation of CFD simulation using RANS turbulence models for building effects on pollutant dispersion*. *Environmental Fluid Mechanics* 6, 181 – 202.

- Water Contact Tank Hydraulics Using Random Packing Material. *Journal AWWA*, 106:2:E98.
- Wilson, J.M. & Venayagamoorthy, S.K., 2010. Evaluation of Hydraulic Efficiency of Disinfection Systems Based on Residence Time Distribution Curves. *Environmental Science & Technology*, 44:24:9377.
- World Chlorine Council, WCC. 2008. *Drinking Water Chlorination*.
- Wright, N.G. & Hargreaves, D.M. 2001. The Use of CFD in the Evaluation of UV Treatment Systems. *Journal of Hydroinformatics*, 3:2:59.
- Xu, Q. 2010. Internal Hydraulic of Baffled Disinfection Contact Tanks Using Computational Fluid Dynamics. Master's thesis, Department of Civil and Environmental Engineering, Colorado State University, Fort Collins, Colorado, USA.
- Yimer, I., Campbell, I., Jiang, L.Y., 2002. *Estimation of the turbulent Schmidt number from experimental profiles of axial velocity and concentration for High-Reynolds-Number Jet Flows*. Canadian Aeronautics and Space Journal 48 (3), 195 - 200.
- Yoshihide, T & Stathopoulos, T., 2007. *Turbulent Schmidt numbers for CFD analysis with various types of flowfield*. Atmospheric Environment 41, 8091–8099.
- Zhang, Y.Q., Arya, S.P., Snyder, W.H., 1996. *A comparison of numerical and physical modeling of stable atmospheric flow and dispersion around a cubical building*. Atmospheric Environment 30, 1327 - 1345.

APPENDIX A

```
#include "udf.h"

DEFINE_DIFFUSIVITY(diff_coeff,c,t,i)
{
return C_MU_T(c,t) / 0.7+0.001;
}
```